Responses to the comments from Reviewer#1

The authors present their analysis of SABER temperature observations to derive gravity wave induced heat fluxes and heating rate between about 20 and 100 km altitude. The authors employ the gravity wave polarization relations to estimate the wave-induced vertical wind fluctuations from SABER observations of the temperature fluctuations. The heat flux and heating rate profiles are then computed and compiled globally over a large latitude range for all 12 months of the year. The paper is well written and organized and the results would be of considerable interest to the atmospheric sciences community. Heat flux observations are difficult to make because they require accurate knowledge of both the wave-driven temperature and vertical wind fluctuations in the atmosphere. In particular, the heat flux depends critically on the phase difference between the wave temperature and vertical wind fluctuations, which is almost, but not quite 90˚. Until now, such observations have only been made by Na Doppler lidars and only in the mesopause region at a handful of locations. Thus, the current study, if valid, would be a significant contribution to our knowledge of gravity effects in the stratosphere, mesosphere and lower thermosphere. Unfortunately, I have serious concerns about the validity of the approach utilized by the authors to derive their heat flux profiles.

Response: First, we greatly appreciate your thorough review of our work and your insightful, constructive suggestions. We acknowledge your serious concerns regarding the validity of our approach to derive the heat flux and heating rate. Our main revisions are outlined as:

(1) We have revised our methodology to account for wave dissipation from the perturbation thermodynamic equation in a dissipative, partially compressible atmosphere, following the method proposed by Weinstock (1983). This approach includes advection, buoyancy forcing, thermal diffusivity, and nonlinear damping rates, providing a more realistic representation of gravity wave dynamics.

(2) We have introduced an effective damping rate $d_{w,eq}$ from energy conservation under steady-state conditions to parameterize the net impact of various dissipative processes. This allows use to derive heat fluxes and heating rate from single SABER temperature profiles but sacrifices the ability to isolate vertical direction-specific wave dissipation and heat flux signatures.

(3) Comparing with the results in the last version, we find following:

- The amplitude of the vertical velocity perturbations in the updated results is smaller than in the previous version.
- The absolute values of the heat fluxes and heating rates are larger compared to those in the previous version.
- The spatiotemporal structures of the new results are highly similar to those of the original, with minimal impact on the overall conclusions.

We address each comment point-by-point. Your comments are shown in black font. Our

responses appear below each comment in blue font, and revisions incorporated into the manuscript are marked in *italic blue font*.

Alongside the point-by-point response, we include the marked-up revised manuscript at the end for reviewer assessment.

1. Non-dissipating gravity waves propagate conservatively in the atmosphere so that the wave amplitude increases with increasing altitude as exp(z/2H), where z is altitude and H is the density scale height. The polarization relations employed by the authors were derived by Vadas (2013) for wave fluctuations scaled by exp(-z/2H) (eq. 13, Vadas, 2013), so indeed the polarization relations apply to pure sinusoidal oscillations given by eq. 1 in the manuscript. However, the authors then apply the polarization relations to a wavelet (see eqs. 5 and 7), which is clearly not a sinusoid. What is the justification for this? More importantly, what errors accrue by assuming that the polarization relation for a wavelet is identical to that for a pure sinusoid?

Response: We appreciate this insightful comment. Our description of the wavelet transform procedure was insufficiently clear in the original manuscript. We note that the polarization relations strictly apply to pure sinusoidal oscillations. To clarify this point, we have added text at the beginning of Section 2.2 in the revised manuscript:

Due to the facts that (1) the polarization relations are strictly derived for pure sinusoidal waves, and (2) the wavelet transform effectively decomposes a signal into monochromatic components, each of which can be treated as a pure sinusoidal wave within the wavelet's support, the wavelet transform allows us to isolate and analyze individual monochromatic components of the signal, which can be approximated as sinusoidal over the localized region. Specifically, the wavelet transform decomposes the total temperature perturbation at each altitude into spectral components associated with individual monochromatic waves. For each extracted monochromatic component of the temperature perturbation, we apply the polarization relations to calculate the corresponding monochromatic vertical velocity perturbation. The full vertical velocity perturbation is then reconstructed via the inverse wavelet transform. The main errors arising during wavelet-based decomposition and reconstruction of monochromatic waves originate from the vertical sampling interval and the adopted vertical wavelength range. For our configuration (0.5 km vertical sampling over 15–110 km altitude, with retained vertical wavelengths of 5–30 km), the wavelet transform effectively isolates monochromatic components, for which the polarization relations hold locally. The local approximation introduces minor errors because each extracted wave packet is nearly monochromatic within the wavelet's support, and these errors are dominated by the finite vertical sampling and wavelength filtering described above rather than departures from the sinusoidal assumption.

Figure R1 shows the $T'(z)$ (dashed line) is reconstructed from $T_{\mathrm{res}}(z)$ (solid line) via Morlet wavelet analysis. It demonstrates that wavelet decomposition and reconstruction preserve the major structures of temperature perturbations while filtering out small-scale perturbations and random noise with wavelengths shorter than 5 km.

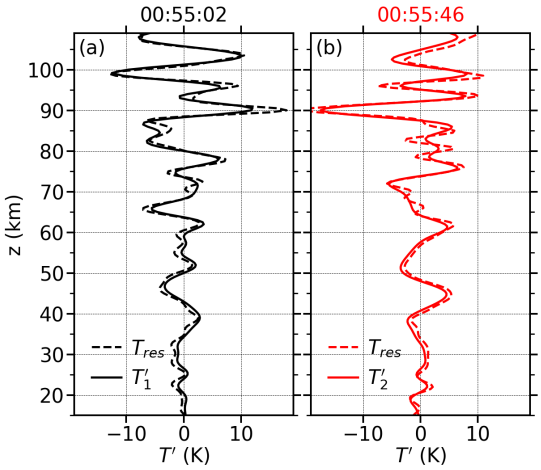


Figure R1. Wavelet decomposition and reconstruction of GW temperature profiles. The two profiles are corresponding to those shown in Figure 1 of the text.

2. A more serious problem is that the Vadas (2013) polarization relations apply only to non-dissipating, fully compressible wave fluctuations, when in fact all waves experience some dissipation (e.g. Guarino et al., 2024; Jandreu et al., 2026, https://doi.org/10.1029/2026GL124048). Furthermore, not all wave fluctuations are fully compressible. Many investigators have argued that the wave fluctuations may be regarded as incompressible (e.g. Walterscheid, 1981; Liu, 2000) and more recently, Gardner (2024, fig. 1, https://doi.org/10.1029/2023JD040436) showed that compressibility varies depending the amount of dissipation. How are the author's results affected by wave dissipation and compressibility? What is the justification for assuming no dissipation and full compressibility?

Response: We appreciate your valuable comments. In the previous version, we did not account for the effects of wave dissipation. This is not reflective of real atmospheric conditions. To address this issue, we derive the heat flux $\overline{w'T'}$ from the perturbation thermodynamic equation in a dissipative, partially dissipative atmosphere (Weinstock, 1983). The compressibility is included through the buoyancy force, which is due solely to the static background compressibility (i.e., the exponential decay of background density with altitude according to scale height H). The detailed revisions are below (Section 2.1 of the new version):

Here, we aim to derived the heat flux and heating rate induced by non-breaking GWs, therefore dissipation effects associated with GWs must be included. Following the method proposed by Weinstock (1983), the heat flux $\overline{w'T'}$ *is derived from the perturbation thermodynamic equation in a*

dissipative, partially compressible atmosphere,

$$\frac{\partial T'}{\partial t} + (u' + \overline{u}) \cdot \nabla T' = -\frac{HN^2}{R} w' + \sigma \nabla^2 T' - d_w T' \tag{1}$$

Equation (1) includes advection due to background wind $\overline{u}$*, buoyancy forcing from compressibility effects, thermal diffusivity* σ *and the nonlinear damping rate* d_w*. However compressible heating associated with velocity divergence* $\nabla u'$ *is omitted. The buoyancy force raises from only the static background compressibility. Specifically, it arises from the exponential decay of background density with altitude according to scale height* $H = R\bar{T}/g$ *with* R *the universal gas constant,* g *gravitational acceleration,* $\bar{T}$ *the background temperature. The squared buoyancy is given by* $N^2 = g/\bar{T}\left(\partial\bar{T}/\partial z + g/c_p\right)$*, where* c_p *is the specific heat at constant pressure. For a monochromic GW, its temperature and vertical velocity perturbations are expressed as,*

$$(T', w') = (A_T, A_w) e^{i(\omega t - kx - mz)} \tag{2}$$

Here, $i = \sqrt{-1}$ *denotes the imaginary unit.* A_T *and* A_w *are complex wave amplitudes. The parameters* ω*,* k*, and* m *correspond to the ground-based frequency, horizontal, and vertical wavenumbers, respectively. Substituting Eq. (2) into Eq. (1) and defining the intrinsic frequency as* $\hat{\omega} = \omega - k\overline{u}$*, we have the polarization relation between* T' *and* w'*,*

$$(i\hat{\omega} + \sigma k_t^2 + d_w) A_T = -\frac{HN^2}{R} A_w \tag{3a}$$

$$A_w = -(i\hat{\omega} + d_\sigma + d_w)\frac{RA_T}{HN^2} = -(i\hat{\omega} + d_\sigma + d_w)\frac{g}{N^2}\frac{A_T}{\bar{T}} \tag{3b}$$

The intrinsic frequency $\hat{\omega}$ *is calculated through the dispersion relation (Fritts and Alexander, 2003),*

$$\hat{\omega}^2 = \frac{k^2 N^2 + f^2(m^2 + 1/4H^2)}{k^2 + m^2 + 1/4H^2} \tag{4}$$

Here, the molecular damping rate $d_\sigma = \sigma k_t^2$ *dependents on the total wavenumber* $k_t^2 = k^2 + m^2$*. The nonlinear damping rate can be approximated by* $d_w = D_{hh}\, k^2 + D_{zz}\, m^2$*, where* D_{hh} *and* D_{zz} *are the eddy diffusivity in the horizontal and vertical directions, respectively.*

However, D_{hh} *and* D_{zz} *cannot be determined directly from existing observations, and they are commonly prescribed via parameterization schemes (Weinstock, 1983). To address this limitation, we propose an effective dissipation rate* $d_{w,eq} = d_\sigma + d_w$ *based on energy conservation and the altitude dependence of* A_T*. For a monochromatic GW, its total wave energy density per unit volume is approximated by* $E \propto A_T^2 \propto e^{z/H_T}$*. Where* H_T *denotes the scale height of* A_T*, defined via* $A_T(z) = A_T(z_0)e^{z/2H_T}$*. Under steady-state condition and energy conservation, the reduction of vertical wave energy flux* F_E *with altitude arises from wave energy dissipation. Using the steady-state vertical energy flux* $F_E = \overline{\rho} c_{gz} E$*, we obtain the energy balance equation:*

$$\frac{dF_E}{dz} = -\overline{\rho} d_{w,eq} E \tag{5}$$

Here, the vertical group velocity c_{gz} *is calculated from Eq. (4),*

$$c_{gz} = \frac{-m\,(\hat{\omega}^2 - f^2)}{\hat{\omega}(k^2 + m^2 + 1/4H^2)^2} \tag{6}$$

For the WKB approximation to hold, the vertical group velocity c_{gz} *must vary slowly with altitude, satisfying* $\left|(dc_{gz}/dz)/c_{gz}\right| \ll |m|$. *This condition permits the approximation* $dc_{gz}/dz \approx 0$. *The background mass density* $\overline{\rho}$ *follows the hydrostatic relation* $d\overline{\rho}/dz = -\overline{\rho}/H$. *Substituting these relations into Eq. (5) yields,*

$$\frac{dF_E}{dz} = \frac{d\overline{\rho} c_{gz} E}{dz} = c_{gz}\overline{\rho}\frac{dE}{dz} + c_{gz}E\frac{d\overline{\rho}}{dz} = c_{gz}\overline{\rho}\frac{E}{H_T} - c_{gz}\overline{\rho}\frac{E}{H} \tag{7}$$

Equating the right-hand sides of Eqs. (5) and (7),

$$-\overline{\rho} d_{w,eq} E = c_{gz}\overline{\rho}\frac{E}{H_T} - c_{gz}\overline{\rho}\frac{E}{H} \tag{8}$$

Canceling common factors $\overline{\rho}E$ *on both sides, we arrive at the effective dissipation rate,*

$$d_{w,eq} = c_{gz}\left(\frac{1}{H} - \frac{1}{H_T}\right) \tag{9}$$

Here $d_{w,eq}$ *denotes an effective dissipation rate, which parameterizes the net impact of processes altering wave amplitude growth. It aggregates the cumulative damping originating from molecular thermal and viscous diffusion, radiative damping in the MLT region, nonlinear wave–wave interactions, and wave saturation due to instabilities. It additionally absorbs residual contributions stemming from minor departures from the WKB approximation and background atmospheric gradients. For SABER observations, the observational filter, which filters out waves with wavelengths shorter than 300–400 km, also partly accounts for the derived effective dissipation rate. Accordingly,* $d_{w,eq}$ *should not be interpreted as a purely molecular or turbulent damping coefficient.*

Notably, the present effective dissipation formulation does not distinguish between upward- and downward-propagating GWs. This marks an important difference from previous studies capable of separating GWs by their upward- and downward-propagation directions (Chu et al., 2022; Gardner, 2024; Guarino et al., 2024; Jandreau and Chu, 2026; Jandreau et al., 2026). The underlying physical difference arises from their respective inversion strategies: those prior studies separate wave components according to their vertical energy propagation direction before computing heat flux and wave dissipation, which permits vertical direction-dependent damping and polarization relations. In contrast, our approach derives a bulk effective dissipation directly from the observed vertical variation of multiple monochromatic wave amplitude envelopes regardless of upward- and downward-propagation directions. This simplification enables direct diagnosis from single SABER temperature profiles but sacrifices the ability to isolate vertical direction-specific wave dissipation

and heat flux signatures.

The horizontal wavenumber is calculated from the phase difference $\Delta\phi$ between two adjacent profiles separated by a horizontal distance of Δx (Alexander et al., 2008; Ern et al., 2004),

$$k = k_a = \Delta\phi/\Delta x \quad (10)$$

Note that $\Delta\phi$ will be calculated in the next subsection. The horizontal wavenumber k_a derived from Eq. (10) is in the along-track direction. The true horizontal wavenumber k_h is therefore given by $k_h = k_a/\cos\alpha$, where α is the angle between the along-track direction and the GW propagation direction. Such that k_h increase as α increases. The uncertainties of α induce uncertainties in the retrieval of w', as well as the resultant heat flux and heating rate. This will be discussed in the next subsection.

Importantly, after implementing the above modifications and recalculations, the amplitude of the vertical velocity perturbation in the updated results is smaller than that in the previous version. Nevertheless, the absolute values of heat fluxes and heating rates are larger compared to those in the previous version. The morphological structures of the old and new results are highly similar.

Figures R2 and R3 display the GW-induced parameters derived using the polarization relations the assumptions of a non-dissipative, fully compressible atmosphere and a dissipative, partially compressible atmosphere, respectively. In Figure R3c, the GW-induced vertical velocity profiles retain the large-scale structures but exhibit reduced magnitudes relative to those in Figure R2c. By contrast, the GW-induced heat fluxes and heating rates in Figures R3d and R3e share similar altitude variations but have larger absolute magnitudes compared to their counterparts in Figures R2d and R2e, respectively.

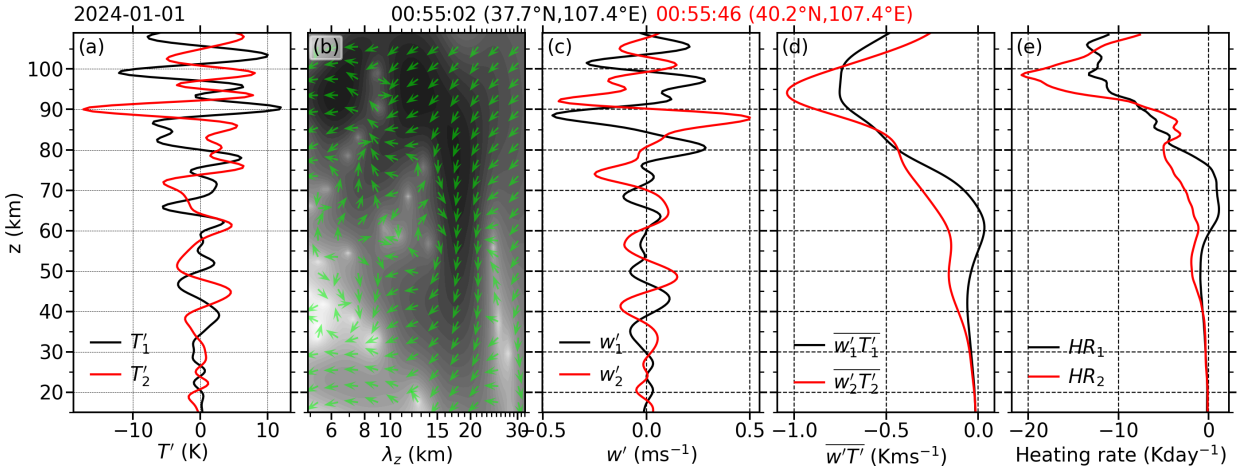


Figure R2. Procedure of deriving GW-induced parameters on 1 January 2024. (a) GW-induced temperature profiles of T_1' (black) at 37.7°N, 107.4°E and T_2' (red) at 40.2°N, 107.4°E. (b) amplitude of $W_{T_1T_2}$ in log10 scale (the magnitudes increase with the darkness), the arrow directions indicate the angles of $\Delta\phi$ (rightward for 0°, upward for 90°, leftward for 180°). (c–e): GW-induced vertical velocity, heat

flux, and heating rate corresponding to T_1' and T_2', respectively.

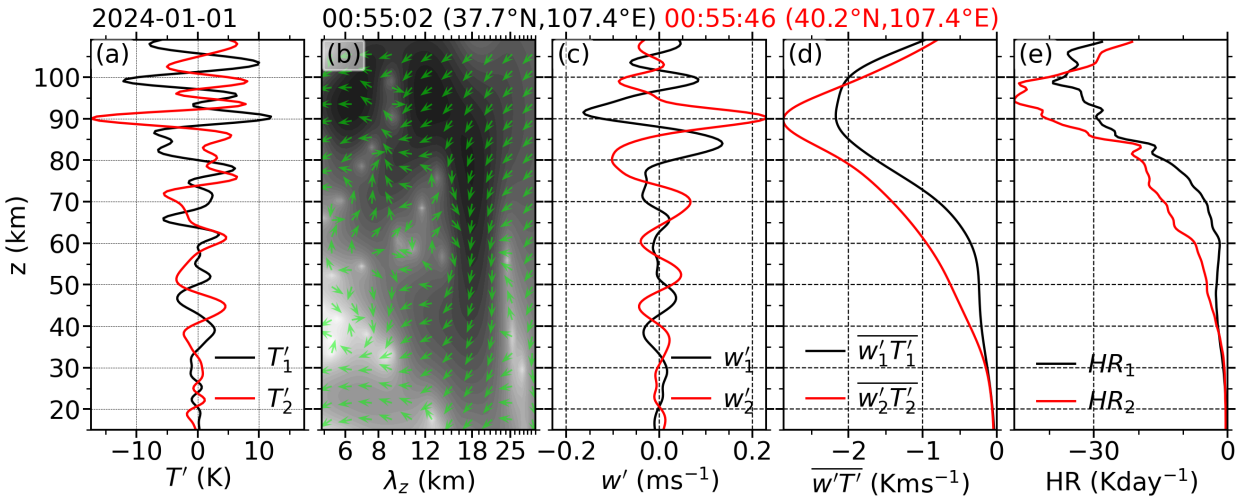


Figure R3. Same caption as Figure R2 but for the GW-induced parameters derived from the perturbed thermodynamic equation in a dissipative, partially compressible atmosphere.

3. As noted previously, the heat flux is strongly dependent on the phase difference between the temperature and vertical wind fluctuations. Chu et al. (2022, eq. 10) used the Vadas (2013) polarization relations to show that for a non-dissipating, fully compressible wave, the sensible heat flux is $\overline{w'T'} \approx -\frac{A_T^2}{2\overline{T}}\frac{\omega}{m}$. For upwardly propagating waves the vertical wave number m is negative, and so the heat flux is positive. Indeed, Chu et al. (2022, fig. 5a) and Gardner & Liu (2007, fig. 6) observed positive heat fluxes with Na Doppler lidars above 95 km where dissipation was expected to be small or moderate. Yet, this same approach, applied to wavelets by the authors, yields negative heat fluxes! Why the difference and how do the authors determine which vertical direction, up or down, their observed wavelets are propagating?

Response: In the previous version, the sign of the vertical wavenumber was incorrectly assigned, leading to an incorrect interpretation of GW propagation directions and heat flux. Lidar observations are advantageous for distinguishing between upward- and downward-propagating GWs using their time–altitude distributions. However, it is difficult to separate upward- and downward-propagating GWs from SABER observations due to the time-spatial aliasing, even along the satellite orbit track. Furthermore, GW dissipation in the MLT must be accounted for. Accordingly, we revised the theoretical framework based on the method proposed by Weinstock (1983) (see the response to comment#2 for detail) to derive vertical velocity perturbations.

We adopted the perturbation thermodynamic equation in a dissipative, partially compressible,

$$\frac{\partial T'}{\partial t} + (u' + \overline{u}) \cdot \nabla T' = -\frac{HN^2}{R} w' + \sigma \nabla^2 T' - d_w T' \qquad (1)$$

Equation (1) includes advection, buoyancy forcing, thermal diffusivity σ and the nonlinear damping rate d_w, while compressible heating associated with velocity divergence $\nabla u'$ is omitted. The buoyancy force raises from only the static background compressibility (i.e., exponential decay of background density with altitude according to scale height H).

The main improvement is the effective damping rate $d_{w,eq}$, which is derived from energy conservation under steady-state conditions. The effective dissipation rate parameterizes the net impact of processes altering wave amplitude growth. It aggregates the cumulative damping originating from molecular thermal and viscous diffusion, radiative damping in the MLT, nonlinear wave–wave interactions, and wave saturation due to instabilities. This formulation additionally absorbs residual contributions stemming from minor departures from the WKB approximation and background atmospheric gradients. For SABER observations, the observational filter, which filters out waves with wavelengths shorter than 300–400 km, also partly accounts for the derived effective dissipation rate. Accordingly, $d_{w,eq}$ should not be interpreted as a purely molecular or turbulent damping coefficient. This simplification enables direct diagnosis from single SABER temperature profiles but sacrifices the ability to isolate vertical direction-specific GW dissipation and heat flux signatures.

4. Lu et al. (2017) measured the phase difference between the T' and w' fluctuations of numerous monochromatic gravity waves between 85 and 100 km and found that the mean phase difference was 2.6° larger than the phase difference predicted by eq. 2. They attributed the difference to wave dissipation. In other words, the additional phase shift introduced by dissipation can lead to negative sensible heat fluxes, but the author's approach of using Vadas (2013) polarization relations for non-dissipating, fully compressible waves cannot produce heat flux observations of real waves that experience dissipation and that may be only partially compressible. Gardner (2024, table 1) derived an approximate solution to the advection-diffusion for heat transfer, which includes the impact of wave dissipation and partial compressibility. Jandreu et al. (2024) adopted this approach to bound the wave-driven thermal diffusivity. Perhaps, the authors could adopt a similar approach to bound the sensible heat flux using their SABER observations.

Response: Thanks for your suggestion. We tested the method from Gardner (2024) and Jandreu et al. (2026) and found that the GW kinetic energy (K_E) depends on the inertial frequency (f) and the fraction of downward-propagating GWs (α_{down}).

$$K_E = \beta(s,q)(1-2\alpha_{down})\frac{\Gamma_{ad} f}{\overline{T}\sqrt{\xi_{inst}}}\left[\frac{Var(T')}{\left(\Gamma_{ad}+\partial\overline{T}/\partial z\right)^2\left[1-(f/N)^{q-1}\right]}\right]^{\frac{3}{2}}$$

$$\beta(s,q) = \begin{cases} \dfrac{2(s+1)}{s}\dfrac{\sqrt{s+1}\,\ln(N/f)}{(s+3)}\left(1-\sqrt{\dfrac{f}{N}}\right) & \text{for } q = 2 \\ \dfrac{(s+1)}{2s}\dfrac{\sqrt{s+1}\left(\sqrt{N/f}-1\right)}{(s+3)}\ln(N/f) & \text{for } q = 3/2 \\ \dfrac{(s+1)(q-1)}{s(q-3/2)}\dfrac{\sqrt{s+1}\,(q-1)\,[(N/f)^{2-q}-1]}{(s+3)(2-q)[1-(f/N)^{q-3/2}]} & \text{for } q \neq 2,\ 3/2 \end{cases}$$

Near the equator, the inertial frequency approaches to zero. This induces undefined terms such as $\ln(N/f)$ and results in zero K_E. Consequently, wave-induced diffusion and heat flux also approaches zero. Additionally, it is difficult to distinguish between upward- and downward-propagating GWs from SABER observations due to the time-spatial aliasing, even along the satellite orbit track. For these reasons, we do not employ this method.

Alternatively, following your recommendation and the approach described in Gardner (2024), we adopt the advection-diffusion for heat transfer within the perturbed thermodynamic equation proposed by Weinstock (1983). Please refer to our response to Comment #2 for further details.

5. The goal of the author's research is quite important, but I believe their approach of using the polarization relations for non-dissipating, fully compressible gravity wave is fatally flawed. I recommend the paper be returned for major revisions.

Response: Thank you for your valuable feedback and for highlighting the importance of our research goal. We fully understand and appreciate your concerns regarding the use of polarization relations for non-dissipating, fully compressible gravity waves. We agree that this approach has limitations and may not accurately represent real atmospheric conditions, where dissipation and partial compressibility play significant roles.

To address these concerns, we have made substantial revisions to our methodology, incorporating the effects of wave dissipation and partial compressibility. Specifically, we have adopted the approach proposed by Weinstock (1983) to derive the heat flux and heating rates from the perturbation thermodynamic equation in a dissipative, partially compressible atmosphere. This approach accounts for the buoyancy force arising from static background compressibility and includes the effective dissipation rate $d_{w,eq}$, which parameterizes the net impact of various dissipative processes.

(1) We have derived the heat flux $\overline{w'T'}$ from the perturbation thermodynamic equation in a dissipative, partially compressible atmosphere, which includes advection, buoyancy forcing, thermal diffusivity, and nonlinear damping rates. This approach accounts for the effects of wave dissipation and partial compressibility.

(2) We have introduced an effective damping rate$d_{w,eq}$ based on energy conservation under

steady-state conditions. This rate parameterizes the cumulative damping from molecular thermal and viscous diffusion, radiative damping, nonlinear wave-wave interactions, and wave saturation due to instabilities.

(3) We have clarified the justification for applying the polarization relations to wavelets and have provided a detailed explanation of the wavelet decomposition and reconstruction process, which allows us to isolate and analyze individual monochromatic components of the signal.

(4) We have compared our results with previous studies that have successfully separated upward- and downward-propagating GWs and have discussed the limitations of our approach in isolating vertical direction-specific wave dissipation and heat flux signatures.

These revisions have altered the amplitude of the vertical velocity perturbations, resulting in larger values for the heat flux and heating rates. These values are consistent with existing observations and theoretical predictions. Additionally, the spatiotemporal structures of the new results are highly similar to those of the original, with minimal impact on the overall conclusions.

Global spatial and temporal variations of gravity-wave-induced heat fluxes and heating rates based on SABER's observations

Xiao Liu[1, 2], Jiyao Xu[2, 3], Jia Yue[4, 5], Qinzeng Li[2], Zhaoai Yan[2], Yangkun Liu[1], Luiz Fillip Rodrigues Vital[6] and Juliano Moro[7]

[1]School of Mathematics and Statistics, Henan Normal University, Xinxiang, China

[2]State Key Laboratory of Solar Activity and Space Weather, National Space Science Center, Chinese Academy of Sciences, Beijing, China

[3]University of the Chinese Academy of Science, Beijing, China

[4]NASA Goddard Space Flight Center, Greenbelt, MD, USA

[5]Physics Department, Catholic University of America, DC, USA

[6]State University of Paraíba — UEPB, Paraíba, Brazil

[7]National Institute for Space Research - INPE, Santa Maria, Brazil

Corresponding author: Jiyao Xu (xujy@nssc.ac.cn)

Key Points:

- Based on linear gravity wave (GW) theory in a dissipative atmosphere, ~~Global~~ global GW~~gravity wave (GW)~~-induced heat fluxes and heating rates are derived from SABER temperature profiles ~~using linear GW theory~~.
- GW-induced heat fluxes and heating rates correlate with GW amplitudes, producing downward heat fluxes and cooling background atmosphere.
- ~~Maxima~~ Peak values of GW-induced heat fluxes and heating rates occur at summer high latitudes, coinciding with the cold summer mesopause.

Abstract

Gravity waves (GWs) play an important role in balancing the energy budget of the mesosphere and lower thermosphere (MLT) by heating/cooling the background atmosphere. Based on the perturbed thermodynamic equation for a dissipative, partially compressible atmosphere,~~The~~ global heat fluxes and heating rates ~~generated~~ induced by non-breaking GWs are derived from SABER observations during 2002−2025. The derived heat fluxes are mainly downward and cool the background atmosphere, with peaks occurring at 80–100 km. Around 35°N, the monthly mean heat flux and heating rate are ~−~~0.7~~3 Kms^{-1} and ~−~~12~~ 40 $Kday^{-1}$, with standard deviations of ~~~~1.1~~5 Kms^{-1} and ~~~~20~~ 80 $Kday^{-1}$, respectively. Global GW-induced heat fluxes and heating rates exhibit stronger annual and weaker semiannual oscillations, with the stronger peak in the summer hemisphere. Moreover, these quantities show notable interhemispheric and seasonal asymmetries, with larger summer amplitudes occurring at the northern high latitudes. Such interhemispheric asymmetry ~~agrees~~ coincides with the colder summer mesopause at northern high latitudes. ~~However, the~~While our retrieved magnitudes of heat fluxes and heating rates ~~derived here~~ are ~~~0.3−0.5 times the values~~ comparable to –lidar observations ~~and are ~0.5 times the~~ theoretical ~~values~~predictions, several competing bias sources affect the results ~~and breaking GWs~~. ~~These underestimations are induced by t~~U~~he u~~ncertainties of GW horizontal propagation directions, observational filter, and the limited range of GW wavelengths observable by SABER tend to underestimate our retrieved values. Conversely, the unresolved partitioning between upward- and downward-propagating GWs introduces an overestimation bias.

1 Introduction

In the mesosphere and lower thermosphere (MLT), the energy budget is governed by multiple coupled dynamical-chemical processes, such as solar radiative heating, photochemical heating, radiative cooling, eddy and molecular diffusivity heating, and adiabatic heating/cooling (Holton, 1983; Smith, 2004). Among the multiple processes, adiabatic heating/cooling is several times larger than other processes (Smith, 2004; Yue and Wang, 2025) and is driven by the residual meridional circulation, which is caused by breaking gravity waves (GWs) in the MLT (Fritts and Alexander, 2003; Hines, 1960; Holton, 1983). The momentum and heat dissipated by breaking GWs have been studied and parameterized in global circulation models and local numerical model (Fritts, 1984; Lindzen, 1981; Liu et al., 1999; Xue et al., 2012). Another consequence of breaking GWs is their resulting body force, which generates larger-scale secondary GWs, which propagate into a wider spatial range as compared to the primary GWs (Li et al., 2022a; Vadas et al., 2003; Vadas et al., 2018). Relative to breaking GWs, theoretical and recent lidar observations showed that non-breaking GWs, which have coherent structures, can propagate into a wider spatial range and influence atmospheric thermal state along their ray path (Chu et al., 2022; Gardner, 2018; Gardner and Liu, 2007; Liu, 2009; Liu, 2000, 2021; Walterscheid, 1981; Weinstock, 1983; Xu et al., 2003). This raises the question of how to quantify the net heat induced by non-breaking GWs and their effects on atmosphere.

The polarization relations for linear GWs in a compressible atmosphere demonstrate that the phase difference ($\Delta\phi_{wT}$) between vertical wind (w') and temperature (T') perturbations deviates from 90° ~~and is non-orthogonal~~. This non-orthogonal phase difference depends on the vertical wavenumber (m), intrinsic wave frequency ($\widehat{\omega}$) of GW, ~~as well as the~~ stat~~ist~~ic stability, as well as the diffusivity of the atmosphere (Fritts and Alexander, 2003; Vadas, 2013; Walterscheid, 1981; Weinstock, 1983). This ~~non-orthogonal phase difference~~ yields a non-zero heat flux ($\overline{w'T'}$), which is the average of the product ($w'T'$) over one wave period or wavelength. Then the non-zero heat flux heats or cools the background atmosphere depending on the vertical propagation direction of GWs (Chu et al., 2022; Guarino et al., 2024; Jandreau and Chu, 2026; Jandreau et al., 2026). Note that, the polarization relations for linear GWs under Boussinesq approximation yield $\Delta\phi_{wT} = 90°$ in a non-dissipative atmosphere. This orthogonal phase difference yields $\overline{w'T'} = 0$ and zero heating rate. Previous simulation and lidar observations confirmed that $\Delta\phi_{wT}$ deviates from 90° by several degrees (Chu et al., 2022; Lu et al., 2017; Xu et al., 2003). In fact, an early study by Walterscheid (1981) showed that non-breaking GWs in a dissipative atmosphere produce

downward heat flux and cool the background atmosphere ~~within their dissipation layers~~. Under typical MLT conditions, non-breaking GW-induced heating rates are of ~8–25 Kday^{-1}. Such magnitudes depend on the static stability and eddy diffusivity. By simulating the nonlinear propagation of GWs and combining the linear GW saturation theory, Liu (2000) showed that upward-propagating saturated GWs induce heating rates about −36.4 Kday^{-1}. These magnitudes are comparable with those of adiabatic heating/cooling induced by the residual meridional circulation in the MLT (Smith, 2004; Yue and Wang, 2025). Thus, the heat fluxes and heating rates induced by non-breaking GWs have been quantified by ground-based sodium lidar observations in the MLT over several stations. Unless otherwise specified, we discuss the heat fluxes and heating rates induced by non-breaking GWs.

Ground-based sodium lidar observations revealed that the GW-induced heat fluxes and heating rates can be negative or positive depending the upward or downward propagation of GWs. Their magnitudes varied greatly from case to case. Tao and Gardner (1995) adopted the sodium lidar at Haleakala (20.8°N, 156.3°W) and revealed upward heat flux below 93 km and downward heat flux above 93 km. This induces heating rates with a maximum value of ~264 Kday^{-1}. Gardner and Yang (1998) analyzed a total of 65 hours of observations by sodium lidar and showed that the average heat flux was −2.29±0.43 Kms^{-1} and the average heating rate was −30.9±5.3 Kday^{-1} in the MLT. Recently, Guo and Liu (2021) analyzed 400 hours of sodium lidar observations between 2014 and 2017 at the Andes Lidar Observatory (ALO, 30.3°~~N~~S, 70.7°W). They revealed significant annual cycles in heat fluxes, with negative peaks of −2.8 Kms^{-1} occurring in July at altitudes of 88–94 km. The corresponding heating rates peaked at −30 Kday^{-1} during June–August, with an annual average of −6.7 Kday^{-1}. Li et al. (2022b) analyzed the sodium lidar observation at the Hefei station from 2012 to 2021. Their results showed that GW-induced heat fluxes exhibited seasonal fluctuations ranging between −1.2 Kms^{-1} and −2.0 Kms^{-1}, yielding an average heating rate of −35 Kday^{-1}. Chu et al. (2022) compared heat fluxes and their corresponding peak altitudes derived from lidar observations at five stations: SOR (35.0°N), Hefei (32.0°N), Maui (20.7°N), ALO (30.3°S), and McMurdo (77.8°S). The heat flux at McMurdo reached a peak of −3 Kms^{-1} at 84 km, while other stations displayed smaller flux peaks located at 88 km or higher. Errors and spectral range of GWs inhibited in observation are regarded as primary factors responsible for such discrepancies (Chu et al., 2022; Gardner and Liu, 2007; Guo and Liu, 2021; Su et al., 2008).

Nevertheless, GWs span a broad spatial and temporal spectra and depend on geographic locations and seasons, making high-resolution simulations computationally challenging (Becker and Vadas, 2018; Liu et al., 2024; Liu et al., 2014a). Sub-grid breaking GWs are always

represented via GW parameterization schemes to get reasonable results (Guarino et al., 2024; Liu, 2021; Liu et al., 2018; Yiğit and Medvedev, 2009). Theory and ground-based lidar observations have illustrated the importance of non-breaking GWs and should also be quantified in global view. Satellite observations provide global coverage but generally lack the capability to directly resolve vertical wind. To partially resolve the contradiction between the advantage of global coverage and the lack of vertical-wind measurements from satellite observations, we try to derive the GW-induced vertical wind, heat flux and heating rate from satellite measured temperature profile and the theory of linear GWs in a compressible dissipative atmosphere.

The purpose of this work is to derive the global GW-induced heat fluxes and heating rates. A short description of our flowchart is as follows: (1) We extract GW temperature perturbations from the temperature profiles measured by the Sounding of the Atmosphere using Broadband Emission Radiometry (SABER) instrument (Esplin et al., 2023; Russell III et al., 1999). (2) Vertical wind perturbations are derived based on ~~dispersion and polarization relations of linear GW~~the perturbated thermodynamic equation in a dissipative, partially compressible atmosphere (Ern et al., 2004; Fritts and Alexander, 2003; Weinstock, 1983). This idea is slightly different from~~In~~ our previous studies, in which~~the~~ GW-induced wind shears were derived from SABER-measured temperature profiles ~~based on~~using linear GW theory (Liu et al., 2020). (3) The heat flux and heating rate are calculated theoretically from the GW temperature and vertical velocity perturbations by time-averaging over one full wave period.

The remainder of this paper is organized as follows: Section 2 describes the theoretical basis and the procedure ~~of~~ for deriving GW-induced parameters, such as temperature perturbations, vertical velocity perturbations, heat flux and heating rate. Section 3 analyzes ~~the GW induce~~these parameters within a latitude band centered~~the~~ 35°N ~~latitude band~~, along with ~~and~~ their associated uncertainties. Section 4 ~~provides~~ presents the global and monthly morphology of the derived parameters. The discussed in Section 5 covers uncertainties, comparison with lidar observations, and the influences of heating rate on the thermal structure in the MLT ~~are discussed in Section 5~~. Conclusions are summarized in Section 6.

2 Method of deriving GW-induced heat flux and heating rate

Before introducing our methodology, we provide a brief summary of the key features of the temperature profiles measured by SABER. The SABER temperature profiles are from 15 km to 110 km altitude and are collected at 83°N–52°S or 52°N–83°S alternatively every about 60 days. For the Level 2A data, the precision of a single temperature profile increases from ~0.3 K at 15

km to 15 K at 110 km with a vertical resolution of 2 km (Dawkins et al., 2018; Remsberg et al., 2008). The SABER temperature is stable after resolving the issue of algorithm instability (Liu et al., 2026; Mlynczak et al., 2020; Mlynczak et al., 2022; Mlynczak et al., 2023) and is suitable ~~to~~ for studying the dynamics of the middle and upper atmosphere.

2.1 Theoretical basis of deriving GW-induced vertical velocity perturbations

Atmospheric waves exhibit distinct temporal and spatial scales, which enable ~~. This characteristic allows~~ the separation of small-scale temperature perturbations $T_{\mathrm{res}}(z)$. This is achieved by subtracting large-scale wave components (~~e.g.,~~such as tides and planetary waves) and background temperatures from raw observational temperature profiles $T(z)$. Then, the GW-induced temperature perturbations $T'(z)$ can be reconstructed from $T_{\mathrm{res}}(z)$ ~~via~~ through bandpass filtering or spectral decomposition within a predefined vertical wavelength range (Alexander et al., 2008; Liu et al., 2017; Liu et al., 2014b; Wang and Alexander, 2010; Yamashita et al., 2013).

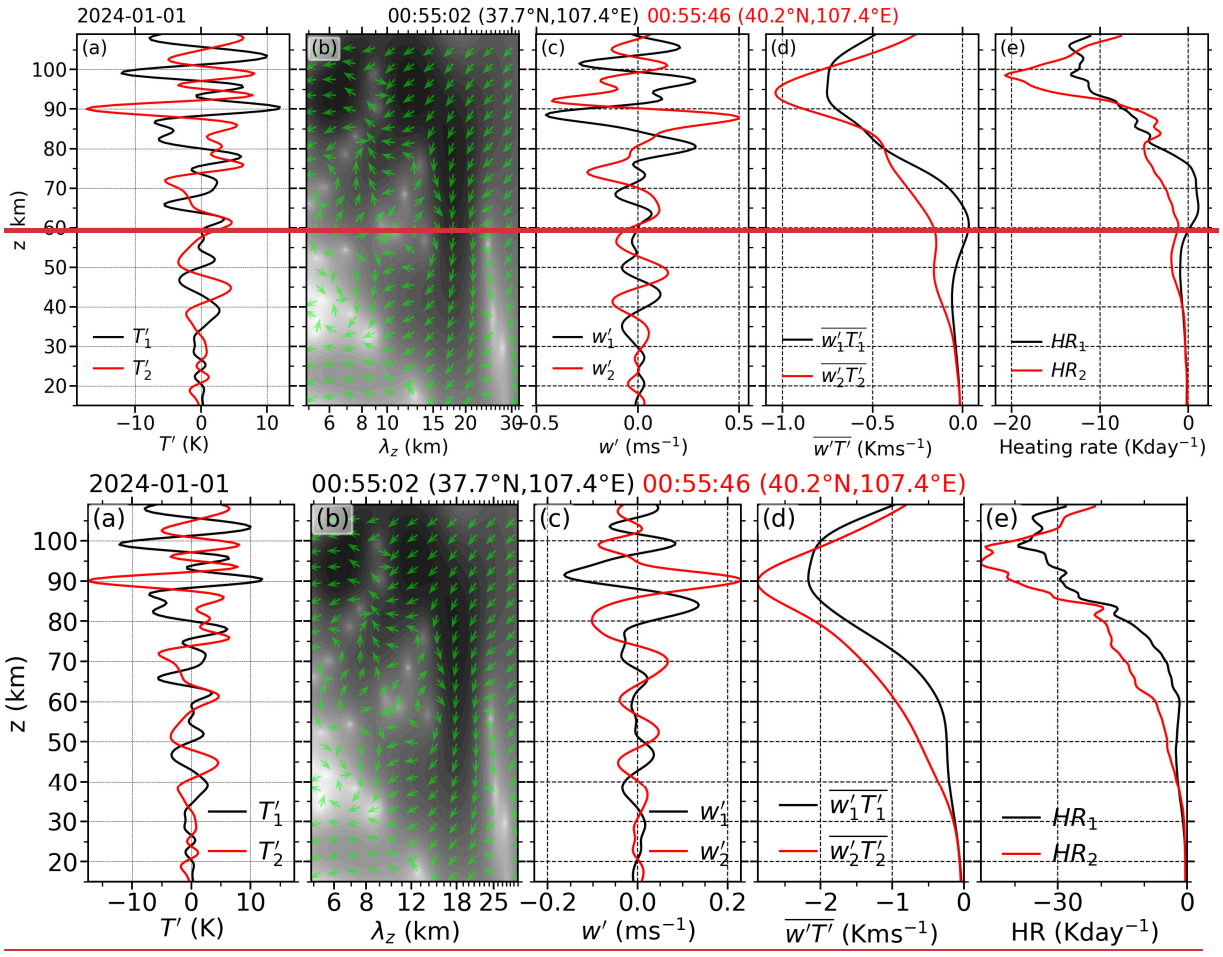


Figure 1. Procedure of deriving GW-induced parameters on 1 January 2024. (a) GW-induced temperature

profiles of T_1' (black) at 37.7°N, 107.4°E and T_2' (red) at 40.2°N, 107.4°E. (b) amplitude of $W_{T_1T_2}$ in log10 scale (the magnitudes increase with the darkness), the arrow directions indicate the angles of $\Delta\phi$ (rightward for 0°, upward for 90°, leftward for 180°). (c–e): GW-induced vertical velocity, heat flux, and heating rate corresponding to T_1' and T_2', respectively.

Herein, we adopt the method detailed ~~described~~ in Appendix A of Liu et al. (2017) to extract $T'(z)$ from $T(z)$. ~~A brief overview is below f~~For completeness, a brief overview is provided below. First, daily SABER temperatures at ascending and descending nodes are individually selected within a 5° latitudinal band. At each node, latitudinal band and altitude, we decompose $T(z)$ into the background field $\bar{T}(z)$ and harmonic fits $T_{\text{fit}}(z)$ for zonal wavenumbers of 1–6. The residual temperature $T_{\text{res}}(z)$ is calculated as $T(z) - \bar{T}(z) - T_{\text{fit}}(z)$. Second, $T'(z)$ is reconstructed from $T_{\text{res}}(z)$ via Morlet wavelet analysis (Torrence and Compo, 1998). In this step, vertical wavelengths are constrained to 5–30 km. Figure 1(a) shows two adjacent profiles of the derived $T'(z)$ as an example.

~~Following a similar approach used to retrieve GW-induced wind shears~~ Liu et al. (2020) retrieved the GW-induced wind shears using linear GW theory in a non-dissipative, compressible atmosphere. Here, we aim to derived the heat flux and heating rate induced by non-breaking GWs, therefore dissipation effects associated with GWs must be included. Following the method proposed by Weinstock (1983), the heat flux $\overline{w'T'}$ is derived from the perturbation thermodynamic equation in a dissipative, partially compressible atmosphere,

$$\frac{\partial T'}{\partial t} + (u' + \bar{u}) \cdot \nabla T' = -\frac{HN^2}{R} w' + \sigma \nabla^2 T' - d_w T' \quad (1)$$

Equation (1) includes advection due to background wind $\bar{u}$, buoyancy forcing from compressibility effects, thermal diffusivity σ and the nonlinear damping rate d_w. However compressible heating associated with velocity divergence $\nabla u'$ is omitted. The buoyancy force raises from only the static background compressibility. Specifically, it arises from the exponential decay of background density with altitude according to scale height $H = R\bar{T}/g$ with R the universal gas constant, g gravitational acceleration, $\bar{T}$ the background temperature. H). The squared buoyancy, is given by $N^2 = g/\bar{T}\left(\partial\bar{T}/\partial z + g/c_p\right)$, where c_p is the specific heat at constant pressure. For a monochromic GW, its temperature and vertical velocity perturbations are expressed as, ~~we derive GW-induced vertical velocity perturbations $w'(z)$ from SABER temperature observations using the dispersion and polarization relations for linear GWs. The GW-induced temperature and vertical velocity perturbations are expressed as,~~

$$(T', w') = (A_T, A_w)e^{i(\omega t - kx - mz)} \quad (2)$$

~~$T' = A_T e^{i(\omega t - kx - mz - \phi_T)}$ (1a)~~

~~$w' = A_w e^{i(\omega t - kx - mz - \phi_w)}$ (1b)~~

Here, $i = \sqrt{-1}$ denotes the imaginary unit. A_T and A_w are complex wave amplitudes~~, and ϕ_T and ϕ_w are wave phases~~. The parameters ω, k, and m correspond to the ground-based frequency, horizontal, and vertical wavenumbers, respectively. Substituting Eq. (2) into Eq. (1) and defining the intrinsic frequency as $\hat{\omega} = \omega - k\bar{u}$, we have the polarization relation between T' and w',

$$(i\hat{\omega} + \sigma k_t^2 + d_w)A_T = -\frac{HN^2}{R}A_w \quad (3a)$$

$$A_w = -(i\hat{\omega} + d_\sigma + d_w)\frac{RA_T}{HN^2} = -(i\hat{\omega} + d_\sigma + d_w)\frac{g}{N^2}\frac{A_T}{\bar{T}} \quad (3b)$$

The intrinsic frequency $\hat{\omega}$ is calculated through the dispersion relation (Fritts and Alexander, 2003),

$$\hat{\omega}^2 = \frac{k^2N^2 + f^2(m^2 + 1/4H^2)}{k^2 + m^2 + 1/4H^2} \quad (4)$$

Here, the molecular damping rate $d_\sigma = \sigma k_t^2$ dependents on the total wavenumber $k_t^2 = k^2 + m^2$. The nonlinear damping rate can be approximated by $d_w = D_{hh}\,k^2 + D_{zz}\,m^2$, where D_{hh} and D_{zz} are the eddy diffusivity in the horizontal and vertical directions, respectively.

However, D_{hh} and D_{zz} cannot be determined directly from existing observations, and they are commonly prescribed via parameterization schemes (Weinstock, 1983). To address this limitation, we propose an effective dissipation rate $d_{w,eq} = d_\sigma + d_w$ based on energy conservation and the altitude dependence of A_T. For a monochromatic GW, its total wave energy density per unit volume is approximated by $E \propto A_T^2 \propto e^{z/H_T}$. Where H_T denotes the scale height of A_T, defined via $A_T(z) = A_T(z_0)e^{z/2H_T}$. Under steady-state condition and energy conservation, the reduction of vertical wave energy flux F_E with altitude arises from wave energy dissipation. Using the steady-state vertical energy flux $F_E = \bar{\rho}c_{gz}E$, we obtain the energy balance equation:

$$\frac{dF_E}{dz} = -\bar{\rho}d_{w,eq}E \quad (5)$$

Here, the vertical group velocity c_{gz} is calculated from Eq. (4),

$$c_{gz} = \frac{-m\,(\hat{\omega}^2 - f^2)}{\hat{\omega}(k^2 + m^2 + 1/4H^2)^2} \quad (6)$$

For the WKB approximation to hold, the vertical group velocity c_{gz} must vary slowly with altitude,

satisfying $\left|\left(dc_{gz}/dz\right)/c_{gz}\right| \ll |m|$. This condition permits the approximation $dc_{gz}/dz \approx 0$. The background mass density $\overline{\rho}$ follows the hydrostatic relation $d\overline{\rho}/dz = -\overline{\rho}/H$. Substituting these relations into Eq. (5) yields,

$$\frac{dF_E}{dz} = \frac{d\overline{\rho}c_{gz}E}{dz} = c_{gz}\overline{\rho}\frac{dE}{dz} + c_{gz}E\frac{d\overline{\rho}}{dz} = c_{gz}\overline{\rho}\frac{E}{H_T} - c_{gz}\overline{\rho}\frac{E}{H} \tag{7}$$

Equating the right-hand sides of Eqs. (5) and (7),

$$-\overline{\rho}d_{w,eq}E = c_{gz}\overline{\rho}\frac{E}{H_T} - c_{gz}\overline{\rho}\frac{E}{H} \tag{8}$$

Canceling common factors $\overline{\rho}E$ on both sides, we arrive at the effective dissipation rate,

$$d_{w,eq} = c_{gz}\left(\frac{1}{H} - \frac{1}{H_T}\right) \tag{9}$$

Here $d_{w,eq}$ denotes an effective dissipation rate, which parameterizes the net impact of processes altering wave amplitude growth. It aggregates the cumulative damping originating from molecular thermal and viscous diffusion, radiative damping in the MLT region, nonlinear wave–wave interactions, and wave saturation due to instabilities. It additionally absorbs residual contributions stemming from minor departures from the WKB approximation and background atmospheric gradients. For SABER observations, the observational filter, which filters out waves with wavelengths shorter than 300–400 km, also partly accounts for the derived effective dissipation rate. Accordingly, $d_{w,eq}$ should not be interpreted as a purely molecular or turbulent damping coefficient.

Notably, the present effective dissipation formulation does not distinguish between upward- and downward-propagating GWs. This marks an important difference from previous studies capable of separating GWs by their upward- and downward-propagation directions (Chu et al., 2022; Gardner, 2024; Guarino et al., 2024; Jandreau and Chu, 2026; Jandreau et al., 2026). The underlying physical difference arises from their respective inversion strategies: those prior studies separate wave components according to their vertical energy propagation direction before computing heat flux and wave dissipation, which permits vertical direction-dependent damping and polarization relations. In contrast, our approach derives a bulk effective dissipation directly from the observed vertical variation of multiple monochromatic wave amplitude envelopes regardless of upward- and downward- propagation directions. This simplification enables direct diagnosis from single SABER temperature profiles but sacrifices the ability to isolate vertical direction-specific wave dissipation and heat flux signatures.

~~For a compressible, f-plane, and non-dissipative atmosphere, the polarization relation linking w' and T' is written as (Chu et al., 2022; Vadas, 2013),~~

$$A_w = \mathcal{P}(\hat{\omega}, m)\frac{A_T}{\bar{T}} \quad (2a)$$

$$\mathcal{P}(\hat{\omega}, m) = \frac{-ig\hat{\omega}}{N^2}\left[1 - \frac{i}{mH}\left(\frac{1}{2} - \frac{1}{\gamma}\right)\right] \Big/ \left[1 + \frac{i}{mH}\left(\frac{1}{2} - \frac{\gamma - 1}{\gamma}\frac{\hat{\omega}^2}{N^2}\right)\right] \quad (2b)$$

~~In this equation, $\mathcal{P}(\hat{\omega}, m)$ is the polarization coefficient. g is the gravitational acceleration, N the buoyancy frequency, and H the atmospheric scale height. The parameter γ is the specific heat ratio of dry air. The intrinsic frequency satisfies:~~

$$\hat{\omega}^2 = \frac{k^2N^2 + f^2(m^2 + 1/4H^2)}{k^2 + m^2 + 1/4H^2} \quad (3)$$

The horizontal wavenumber is calculated from the phase difference $\Delta\phi$ between two adjacent profiles separated by a horizontal distance of Δx (Alexander et al., 2008; Ern et al., 2004),

$$k = k_a = \Delta\phi/\Delta x \quad (410)$$

Note that $\Delta\phi$ will be calculated in the next subsection. ~~the~~ The horizontal wavenumber k_a derived from ~~Equation~~ Eq. (410) is in the along-track direction. The true horizontal wavenumber k_h is therefore given by $k_h = k_a/\cos\alpha$, where α is the angle between the along-track direction and the GW propagation direction. Such that k_h increase as α increases. ~~For instance, if $\alpha = 60°$, $k_h = 2k_a$, the true intrinsic frequency $\hat{\omega}_h$ is approximately $2\hat{\omega}_a$, here $\hat{\omega}_a$ is the intrinsic frequency calculated from Equations (3) and (4).~~ The uncertainties of α induce uncertainties in the retrieval of w', as well as the resultant heat flux and heating rate. This will be discussed in the next subsection.

2.2 GW-induced vertical velocity perturbations, heat fluxes, and heating rate

Due to the facts that (1) the polarization relations are strictly derived for pure sinusoidal waves, and (2) the wavelet transform effectively decomposes a signal into monochromatic components, each of which can be treated as a pure sinusoidal wave within the wavelet's support, the wavelet transform allows us to isolate and analyze individual monochromatic components of the signal, which can be approximated as sinusoidal over the localized region. Specifically, the wavelet transform decomposes the total temperature perturbation at each altitude into spectral components associated with individual monochromatic waves. For each extracted monochromatic component of the temperature perturbation, we apply the polarization relations to calculate the corresponding monochromatic vertical velocity perturbation. The full vertical velocity perturbation is then

reconstructed via the inverse wavelet transform. The main errors arising during wavelet-based decomposition and reconstruction of monochromatic waves originate from the vertical sampling interval and the adopted vertical wavelength range. For our configuration (0.5 km vertical sampling over 15–110 km altitude, with retained vertical wavelengths of 5–30 km), the wavelet transform effectively isolates quasi-monochromatic components, for which the polarization relations hold locally. The local approximation introduces minor errors because each extracted wave packet is nearly monochromatic within the wavelet's support, and these errors are dominated by the finite vertical sampling and wavelength filtering described above rather than departures from the sinusoidal assumption. We derive the $w'(z)$ from $T'(z)$ based on the aforementioned theory and Morlet wavelet analysis (Torrence and Compo, 1998).

The wavelet transform of $T'(z)$ takes the form:

$$W_T(a,z) = \frac{1}{\sqrt{a}} \int_{-\infty}^{\infty} T'(\tau)\, \psi^* \left(\frac{\tau - z}{a} \right) d\tau \qquad (5a11a)$$

with the Morlet mother wavelet of

$$\psi(z) = \pi^{-1/4} e^{ik_0 z} e^{-z^2/2} \qquad (511b)$$

Here, $\psi^*(z)$ is the complex conjugate of $\psi(z)$, and k_0 is the central wavenumber. The wavelet scale a relates to the physical wavelength λ and the vertical step Δz via $a = \lambda k_0 / 2\pi\Delta z$. Using ~~Equation~~ Eq. (511), the wavelet coefficients $W_{T_1}(a,z)$ and $W_{T_2}(a,z)$ are calculated from $T_1'(z)$ and $T_2'(z)$, respectively. The phase difference $\Delta\phi(a,z)$ between $T_1'(z)$ and $T_2'(z)$ is calculated as,

$$W_{T_1T_2}(a,z) = W_{T_1}(a,z) \cdot W_{T_2}^*(a,z) \qquad (612a)$$

$$\Delta\phi(a,z) = \tan^{-1}\arg\left[W_{T_1T_2}(a,z)\right] \qquad (612b)$$

Figure 21(b) shows the amplitude of $W_{T_1T_2}(a,z)$ and the phase difference between $T_1'(z)$ and $T_2'(z)$. The horizontal wavenumber k_a is calculated from $\Delta\phi(a,z)$ by ~~Equation~~ Eq. (410). The intrinsic frequency $\hat{\omega}_a$ is calculated by Eq.~~uation~~ (34). Substituting these parameters into ~~Equation~~ Eq. (23) and using the effective dissipation rate $d_{w,eq} = d_\sigma + d_w$ calculated by Eq. (9), the wavelet coefficient of $w'(z)$ is written as,

$$W_w(a,z) = -\left(i\hat{\omega} + d_{w,eq}\right) \frac{g}{N^2} \mathcal{P}\left(\hat{\omega}(a), m(a)\right) \cdot \frac{W_T(a,z)}{\overline{T}(z)} \qquad (713)$$

Finally, $w'(z)$ is reconstructed via the inverse wavelet transform of $W_w(a,z)$,

$$w'(z) = \frac{dj\sqrt{\Delta z}}{C_\delta\, \psi_0} \sum_{j=j_{\min}}^{j_{\max}} \frac{\mathrm{Re}\left[W_w(a_j,z)\right]}{\sqrt{a_j}} \qquad (814)$$

Here, $C_\delta = 0.776$ is the reconstruction constant. The summation indices $j_{\min}$ and $j_{\max}$ correspond

to the scale bounds $a_{\min}$ and $a_{\max}$, which are converted from the wavelength interval $[\lambda_{\min}, \lambda_{\max}]$ with $\lambda_{\min} = 5$ km and $\lambda_{\max} = 30$ km. The vertical velocity perturbation profiles derived from $T_1'(z)$ and $T_2'(z)$ are displayed in Figure 1(c).

The GW-induced heat flux $\overline{w'T'}$ is defined as the period-averaged product of $w'T'$. The real-valued GW solutions are the real parts of ~~Equation~~ Eq. (~~1~~2):

$$T' = A_T \cos(\omega t - kx - mz - \phi_T) \quad (9a)$$

$$w' = A_w \cos(\omega t - kx - mz - \phi_w) \quad (9b)$$

Thus, at each spatial location (x, z), the period-averaged heat flux $\overline{w'T'}$ can be analytically derived by integrating the instantaneous covariance $w'T'$ over one wave period $2\pi/\omega$,

$$\overline{w'T'}(z) = \frac{\omega}{2\pi}\int_0^{2\pi/\omega} T'(t)w'(t)dt = \frac{1}{2}A_w A_T \cos(\Delta\phi_{wT}), \Delta\phi_{wT} = \phi_w - \phi_T \quad (10)$$

The wavelet coefficients of $w'(z)$ and $T'(z)$ are denoted as $W_w(a, z)$ and $W_T(a, z)$, respectively. For monochromatic harmonic waves, the scale-resolved wavelet flux can be written as,

$$F(a, z) = \frac{1}{2}\mathrm{Re}[W_w W_T^*] = \frac{1}{2}|W_w||W_T|\cos(\Delta\phi_{wT}) = \frac{1}{2}A_w A_T \cos(\Delta\phi_{wT}) \quad (11)$$

Here, $F(a, z)$ is the period-averaged heat flux contributed by the individual wave component corresponding to wavelet scale a at altitude z. The equality between the wavelet-derived term and the analytical flux (the last "=" of ~~Equation~~ Eq. ~~11~~17) holds due to the two properties of the Morlet wavelet transform for harmonic signal. First, the modulus of wavelet coefficients is linearly proportional to physical wave amplitudes. Second, the retrieved phase difference agrees exactly with that of the original signal. The proportionality coefficient is fully removed via wavelet normalization during reconstruction.

To obtain the altitude-dependent total heat flux from multi-scale GW components, we integrate the scale-resolved flux $F(a, z)$ over all scales. The integration is weighted by $\Delta a_{kj}/a_{kj}^2$ and normalized by C_ψ:

$$\overline{w'T'}(z) = \frac{1}{C_\psi}\sum_{jj=j_{\min}}^{j_{\max}}\left[F(a_k, z)\cdot\frac{\Delta a_{kj}}{a_{kj}^2}\right] \quad (12)$$

The vertical distributions of GW-induced heat flux derived from $T_1'(z)$ and $T_2'(z)$ are shown in Figure 1(d). The results show that the GW-induced heat flux is predominantly negative with peaks around 85 km. ~~This indicates a downward transport of heat by upward propagating GWs.~~ The GW-induced heating rate (HR) is further calculated as (Gardner and Yang, 1998; Weinstock, 1983),

$$HR = \frac{\partial T}{\partial t} = -\frac{1}{\bar{\rho}}\frac{\partial(\bar{\rho}\overline{w'T'})}{\partial z} \quad (13)$$

Here, $\bar{\rho}$ is the background density, which is derived in the same manner as the background temperature $\bar{T}$. Figure 1(e) shows the heating rates induced by $T_1'(z)$ and $T_2'(z)$, respectively. The results show that the heating rates are mainly negative with peaks around 90 km. This feature indicates that GW-induced perturbations effectively cool the background atmosphere in this region at least in this case.

3 The retrieved parameters and uncertainty analysis

In this section, we first ~~show~~ present GW-induced parameters around 35°N with an offset of ±5° for June and December. This latitude band is well-sampled by lidar measurements. ~~These~~ The presented parameters include relative temperature perturbation, vertical velocity perturbation, heat flux and heating rate. ~~Then~~Next, we compare these retrieved parameters ~~are compared~~ against their lidar-derived counterparts~~. T~~ to quantify the discrepancies between our retrievals and lidar results~~,~~. Finally, we conduct theoretical analysis to assess how the ~~influences of~~ angle α influences~~affects~~ the uncertainties of the GW-induced parameters.

3.1 Retrieved parameters at 35°N

Figures 2(a1–d1) ~~shows~~ present the amplitudes of the GW-induced relative temperature ($|T'/\bar{T}|$) and vertical velocity ($|w'|$) perturbations, and the values of $\overline{w'T'}$ and ~~GHR~~ at 35°N in June. The mean values of these GW-induced parameters ~~of~~ in December are also ~~shown~~ presented in Figures 2(a2–d2). Since the variation of $|T'/\bar{T}|$ serves as the fundamental for deriving the other parameters, we first conduct a detailed analysis of this variable. Figure 2(a1) shows that $|T'/\bar{T}|$ exhibits substantial variability across individual profiles at every altitude. Their magnitudes increase from below to about 100 km and then decrease above 100 km. Notably, ~~T~~the 50th percentile (P50) magnitudes of $|T'/\bar{T}|$ are generally smaller than their arithmetic mean values. This indicates that the magnitudes of $|T'/\bar{T}|$ are predominantly distributed at small magnitudes, while extremely large outliers positively skew the mean above the P50.

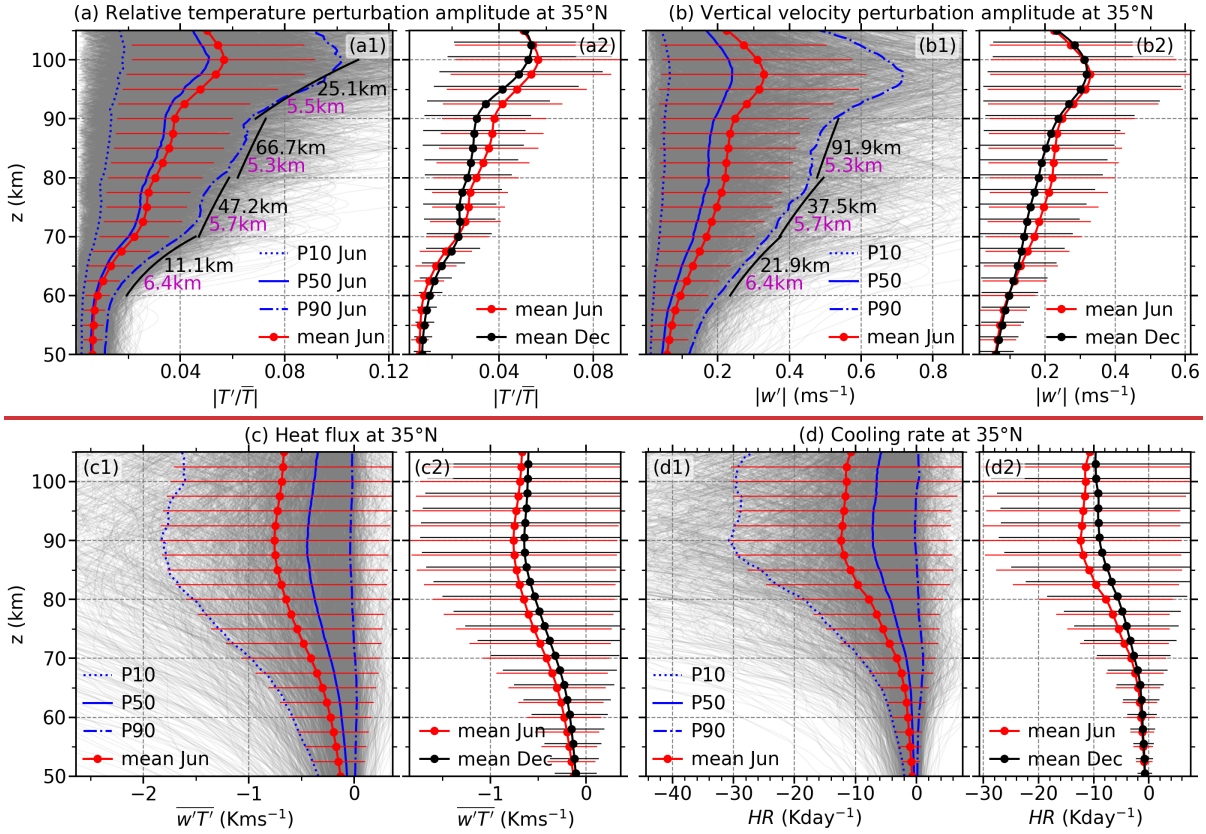
In ~~G~~general~~ly~~, the mean, P10, P50 and P90 profiles of $|T'/\bar{T}|$ exhibit similar altitude variations. This indicates that the vertical variations of $|T'/\bar{T}|$ are almost homogeneous across different statistical quantiles, despite the positively skewed distribution of individual profiles. It is worth noting that percentiles are calculated from absolute values of wave amplitudes, heat flux, and heating rate to facilitate intercomparison. This yields a unified statistical metric: P90 is adopted consistently for all variables, eliminating the need to use P10 separately for heat flux and heating rate, which are predominantly negative.

To quantify the gradient of vertical variations of $|T'/\bar{T}|$, we employ an exponential ~~fit the P90 of $|T'/\bar{T}|$ by a~~ function ~~of~~ $\exp(z/2H_A)$ to fit the P90 of $|T'/\bar{T}|$ ~~by a~~at four altitude ranges (~~i.e.,~~ 60–70 km, 70–80 km, 80–90 km, and 90–100 km). Here H_A is the corresponding scale height. A larger value of H_A indicates a slower increase ~~of~~ in the P90 of $|T'/\bar{T}|$. Figure 2(a1) shows ~~that~~ the fitting results (black line) and the magnitudes of H_A at the four altitude ranges. Additionally, ~~T~~the scale heights ~~H_T~~H, which are calculated from averaged background temperature at the four altitude ranges, are ~~also~~ labeled by ~~a~~ magenta numbers. We see that the magnitudes of H_A are larger than those of ~~H_T~~H by a factor of 2–12 times. Moreover, the magnitudes of H_A are largest at 80–90 km, and are larger at 70–80 km and are smallest at 60–70 km. This indicates that ~~the~~ GWs dissipate~~d~~ throughout ~~the~~ this altitude range. ~~While t~~The strongest dissipation occurs at ~70–90 km, ~~where~~ which ~~is just below the mesopause and~~ coincides with persistent layers of GW dissipations (Liu et al., 2022).

Above 100 km, the magnitudes of $|T'/\bar{T}|$ decrease with ~~the~~ increasing altitude due to several reasons. ~~This is because~~First, molecular viscosity and thermal diffusivity become important factors in~~in~~ dissipating GWs at higher altitudes (Liu et al., 2013; Ortland and Alexander, 2006; Vadas and Fritts, 2005; Xu et al., 2009). Consequently, ~~O~~only waves with longer vertical wavelengths can propagate into ~~a~~ higher altitudes (Liu et al., 2013; Vadas and Fritts, 2005). Second,~~This is because of~~ wavelet edge effects can introduce artificial features and lead to signal power loss during GW extraction from SABER temperature ~~measurements~~profiles. To mitigate these issues, we limit our analysis to altitudes below ~~We do not analyze GWs extracted from SABER temperature above~~ 100 km and do not consider GWs extracted above this altitude range.

~~Although~~ While the vertical variations of $|w'|$ in ~~Figure~~ Fig. 2(b) share some similarities with~~exhibit similar variations to~~ those of $|T'/\bar{T}|$ ~~generally~~, ~~their~~ there are two main differences that can be attributed to two distinct factors~~ascribed to~~: ~~(1)~~First, ~~T~~the scale heights of ~~the~~ P90 ~~of~~ for $|w'|$ are generally larger than those of $|T'/\bar{T}|$, except at 70–80 km. This difference is largely due to the fact that~~As shown in Equations (2) and (3),~~ $|w'|$ is proportional to ~~the~~ intrinsic frequency and effective damping rate (Eq. 3b) ~~and thus the vertical wavelength (Chu et al., 2022; Vadas, 2013)~~. Compared to $|T'/\bar{T}|$, $|w'|$ is more sensitive to high-frequency GWs and damping rate (Geller and Gong, 2010). ~~Thus~~As a result, ~~a sharper dissipation of~~ $|w'|$ undergoes stronger dissipation with altitude due to ~~with altitudes is caused by the stronger~~enhanced dissipation of low-frequency GWs ~~having lower frequency and~~with shorter vertical wavelengths (Vadas and Fritts, 2005). ~~(2)~~Second, ~~T~~the peaks of $|w'|$ ~~are mainly~~occur around 96 km, which is slightly lower than

the ~100 km peaks ~~of~~ observed for $|T'/\bar{T}|$~~, which are around 100 km~~. This difference ~~is mainly~~ can be attributable to~~caused by~~ phase difference $\Delta\phi_{wT}$ between w' and $T'/\bar{T}$ ~~as shown in Equation (2)~~, which deviates from 90° by several degrees (Chu et al., 2022; Lu et al., 2017; Weinstock, 1983; Xu et al., 2003).



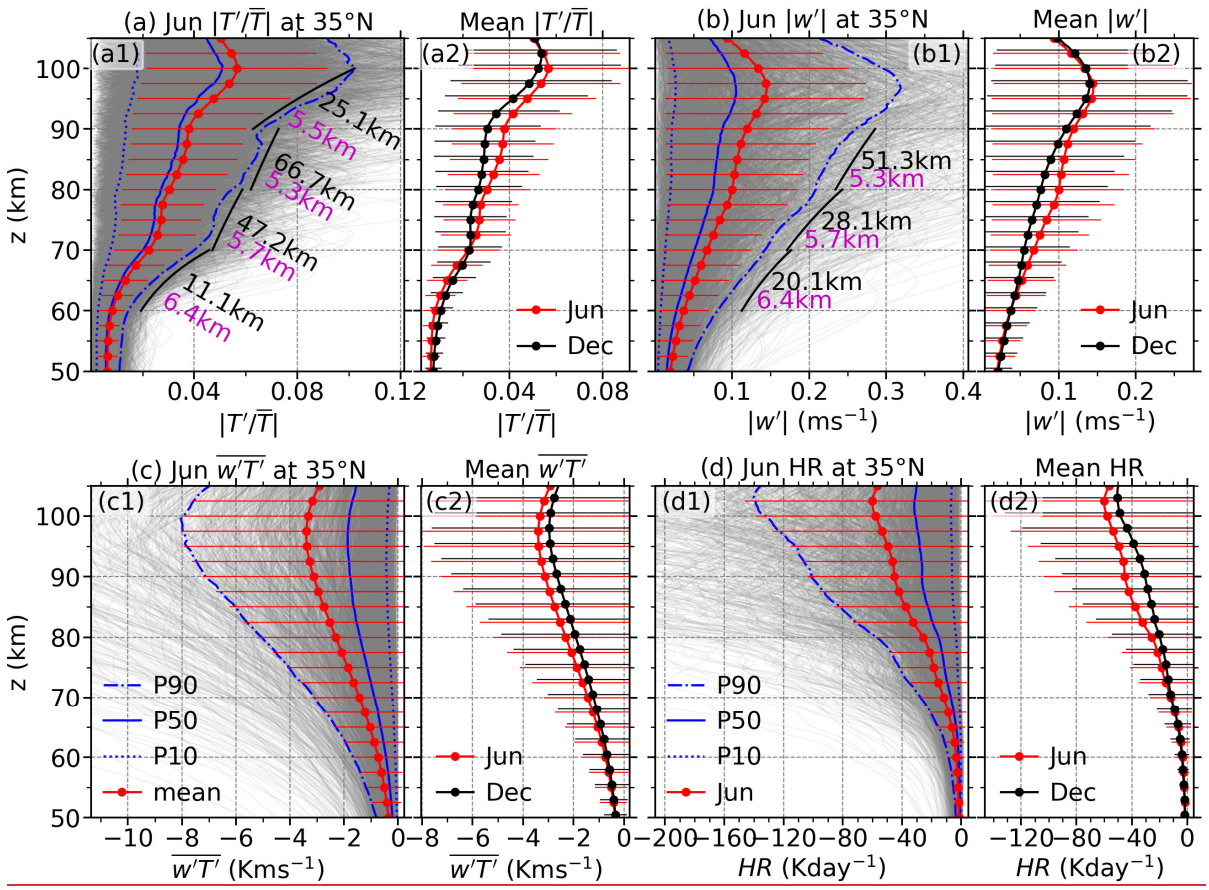


Figure 2. Overlaid profiles of the GW-induced parameters and their statistical quantiles at 35°N in June and December 2024. (a1): Profiles of $|T'/\bar{T}|$ (grey lines) and their statistics, i.e., 10th (P10: blue dot), 50th (P50: blue solid), 90th (P90: blue dash-dot) percentiles and the means (red line) and standard deviations (red error bar). (a2) The means and standard deviations of $|T'/\bar{T}|$ in June (red) and December (black). (b1–d1): same caption as (a1) but for $|w'|$, $\overline{w'T'}$, and ~~GHR~~, respectively. (b2–d2): same caption as (a2) but for $|w'|$, $\overline{w'T'}$, and ~~GHR~~, respectively.

Figures 2(c) and 2(d) ~~show that~~real significant variations in ~~the~~ heat fluxes and heating rates ~~exhibit large variability from one profile to another~~across individual profiles and with altitude. Notably, ~~Their~~these ~~magnitudes~~ values are predominantly~~mainly~~ negative, ~~which~~ indicat~~es~~ing that ~~the upward propagating~~ GWs induce downward heat fluxes and cool the background atmosphere within a dissipative, partially compressible atmosphere. The statistical quantiles of heat fluxes and heating rates decrease ~~with altitude~~ sharply with altitude below ~90 km, followed by a gradual increase above this altitude~~ and then increase with altitude slowly above ~90 km~~. ~~These~~ This ~~altitude~~ vertical variation~~s are~~ differ~~sent~~ from those ~~of~~ observed in $|T'/\bar{T}|$ and $|w'|$ at ~90–100 km, because ~~the~~ heat fluxes and heating rates ~~are related to~~depend on both the amplitudes of $|T'/\bar{T}|$ and $|w'|$ and their phase differences ~~between $|T'/\bar{T}|$ and $|w'|$~~. The mean values for ~~The h~~heat

fluxes ~~have mean values of~~are ~~−0.7~~3 Kms^{-1} with standard deviations of ~~1.1~~5 Kms^{-1} ~~at~~ over 80–100 km. Similarly, the mean values for ~~The h~~heating rates ~~have mean values of~~are ~~−12Kday~~40 Kday^{-1} with standard deviations of ~~20~~ 80 Kday^{-1}. The magnitudes of the P50 ~~of~~ for heat fluxes and heating rates are ~0.6 times ~~of~~ their respective mean values. ~~While~~ Whereas, the ~~magnitudes of~~ P90 magnitudes~~of heat flux and heating rate~~ are ~~of~~ roughly 2.5 times ~~of~~ larger than their respective mean values. This indicates that both sample distributions exhibit ~~both heat flux and heating rate have~~ negatively ~~skewed~~skewness ~~distributions of individual samples~~. Figures 2(a2–d2) show that retrieved absolute magnitudes~~the absolute values of retrieved parameters~~ are larger in June ~~than those in~~compared to December above 70 km. This indicates that the seasonal variations in GW strength drive the corresponding seasonal changes in~~induce similar variations of~~ heat fluxes and heating rates, highlighting the importance of considering these fluctuations when modeling atmospheric dynamics.

3.2 Comparison with observations ~~and theoretical analysis~~

Sodium lidar can measure temperature and three-dimensional winds with high spatial and temporal resolutions. This enables the retrieval of GW-induced heat flux and heating rate. Based on 65 hours of sodium lidar observations over seven nights at Starfire Optical Range (SOR; 35°N, 107°W), Gardner and Yang (1998) derived a mean heat flux of −2.3±0.43 Kms^{-1} and a corresponding heating rate of −30.9 ±5.2 Kday^{-1}. A further analysis of 370 hours of SOR lidar observations in 1998−2000 revealed that the monthly mean heat flux exhibits semiannual variations with winter peaks of −3 Kms^{-1} and summer peaks of −1.5 Kms^{-1} around 88 km. Meanwhile, the heating rate reaches seasonal maxima of −100 Kday^{-1} in winter and −80 Kday^{-1} in summer around 90 km (Gardner and Liu, 2007). Using temperature and winds observed by a sodium lidar at Colorado State University (40.6°N, 105°W) on December 3, 2004, Li et al. (2007) investigated the heating rate associated with GW breaking. Their results indicate that the heating rate is positive between 94 and 98 km, with a maximum value of 62.4 Kday^{-1} around 96 km. Above 98 km, however, the heating rate turns negative, reaching a minimum peak of −36 Kday^{-1} near 100 km. Using 400 hours of sodium lidar observations in 2014−2017 at Andes Lidar Observatory (ALO; 30°S, 71°W), Guo and Liu (2021) showed that the heat flux is downward throughout the year below 95 km and has a peak of −3 Kms^{-1} in July. The corresponding heating rate reaches its annual peak of −30 Kday^{-1} around July. Using 400 hours of sodium lidar observations in 2012−2021 at Hefei (32°N, 117°E), Li et al. (2022b) showed that the heat flux varies from −1.2 Kms^{-1} to −2 Kms^{-1} throughout the year below 94 km. The annual heat flux has peak of −2 Kms^{-1}

at 89 km. In the 87−95 km, the mean heating rate is approximately −35 Kday^{-1}, with a peak value of around −50 Kday^{-1} near 90 km. Furthermore, Chu et al. (2022) compared the heat flux and its peak altitudes based on lidar observations at five stations, including SOR (35.0°N), Hefei (32.0°N), Maui (20.7°N), ALO (30.3°S), and McMurdo (77.8°S). Their results showed that the peak heat flux at McMurdo is the strongest and reaches −3 Km s^{-1} at an altitude of 84 km, whereas the peaks heat fluxes at the remaining stations were smaller and occurred at altitudes of 88 km or above.

The magnitudes of the ~~above~~ lidar-derived heat flux and heating rate are mainly around their peak altitude. The heat fluxes are from −1.2 to −3 Kms^{-1} at altitudes ranging from 84 to 90 km. The corresponding heating rates are from −30 to −100 Kday^{-1} around 90 km. It should be noted that the magnitudes of heat fluxes and heating rates may be influenced by observation errors and the spatial and temporal spectral ranges of GWs resolved by observations (Gardner and Liu, 2007; Guo and Liu, 2021; Su et al., 2008). Using ~~the~~ a linear dispersion relation for GWs and considering eddy and molecular diffusion, Weinstock (1983) derived ~~the~~ relationships between heat flux and vertical diffusivity D_{zz}. Specifically,~~,~~

$$\overline{w'T'} = -(H_T N^2/R) D_{zz} \qquad (\text{~~14~~20}a)$$

Then the heating rate is expressed as,

$$HR \approx -(N^2/R) D_{zz} \qquad (\text{~~14~~20}b)$$

For the typical values of $H_T = 5.5$ km, buoyancy frequency $N = 0.02\ \mathrm{s}^{-1}$, gas constant $R = 287\ \mathrm{Jkg}^{-1}\mathrm{K}^{-1}$ and $D_{zz} = 200\ \mathrm{m}^2\mathrm{s}^{-1}$ in the MLT, Equation (20~~4~~) predicts the heat flux and heating rate are about −1.5 Kms^{-1} and ~−24 Kday^{-1}. Generally, the magnitudes of heat fluxes and heating rates retrieved from SABER temperature measurements are ~~~0.3−0.5 times~~comparable ~~of~~ to those retrieved from lidar observations and ~~and are ~0.5 times of~~ the theoretical values.

3.3 Uncertainty analysis

~~The~~ One of the main uncertainties ~~of~~ in the GW-induced vertical velocity, heat flux, and heating rate arises from the ~~undefined~~ unknown angle α. The true horizontal wavenumber k_h and the along-track horizontal wavenumber k_a ~~horizontal wavenumbers~~ are related ~~via~~ by $k_h = k_a/\cos\alpha$. Under the assumptions of $k \ll m$, $4\pi Hm \ll 1$, and $\partial\bar{T}/\partial z \ll g/\text{~~C~~}c_p$, the dispersion relation ~~Equation~~ Eq. (3~~4~~) can be simplified as $\hat{\omega}_h \approx N|k_h|/|m|$. ~~This indicates that~~Therefore, the true intrinsic frequency $\hat{\omega}_h$ relates to the along-track intrinsic frequency $\hat{\omega}_a$ ~~via~~ by $\hat{\omega}_h \approx \hat{\omega}_a/\cos\alpha$. Similarly, the true vertical group velocity $c_{gz,h}$ relates to the along-track group velocity $c_{gz,a}$ by $c_{gz,h} = c_{gz,a}/\cos\alpha$. The equivalent dissipation rate $d_{w,eq}$ depends on the vertical group velocity, thus the true equivalent dissipation rate $d_{w,eq,h}$ relates to the along-track equivalent

dissipation rate $d_{w,eq,a}$ by $d_{w,eq,h} \approx d_{w,eq,h}/\cos\alpha$. The amplitude of vertical velocity is propotional to the intrinsic frequency and the effective damping rate. Consequently, the true vertical velocity amplitude $A_{w,h}$ relates to the along-track vertical velocity amplitude $A_{w,a}$ by $A_{w,h} \approx A_{w,a}/\cos\alpha$.

Based on the above relations, t~~The module of the polarization coefficient is further simplified as $|\mathcal{P}(\hat{\omega}_h, m)| = g\hat{\omega}_h/N^2$ (Chu et al., 2022). This indicates that the true amplitudes A_w^h relates to the along-track amplitudes A_w^a via $A_w^h \approx A_w^a/\cos\alpha$. Based on Equation (10), t~~he true heat flux $\overline{w'T'}_h$ relates to the along-track heat flux $\overline{w'T'}_a$ ~~via~~ by $\overline{w'T'}_h \approx \overline{w'T'}_a/\cos\alpha$. If the angle α does not change with altitude, the true heating rate HR_h relates to the along-track heating rate HR_a via $HR_h \approx HR_a/\cos\alpha$. However, if the angle α changes altitude, the term $\cos\alpha$ should be included in the vertical gradient of $\overline{w'T'}_h$. Thus, we have,

$$\frac{1}{\bar{\rho}}\frac{\partial \bar{\rho}\overline{w'T'}_h}{\partial z} = \frac{1}{\bar{\rho}}\frac{\partial \bar{\rho}}{\partial z}\overline{w'T'}_a + \frac{\partial}{\partial z}\left(\frac{\overline{w'T'}_a}{\cos\alpha}\right) = \frac{1}{H}\overline{w'T'}_a + \frac{1}{\cos\alpha}\frac{\partial \overline{w'T'}_a}{\partial z} + \overline{w'T'}_a\left(\frac{\sin\alpha}{\cos^2\alpha}\right)\frac{d\alpha}{dz} \quad (21)$$

~~$$\frac{1}{\bar{\rho}}\frac{\partial \overline{w'T'}_h}{\partial z} = \frac{1}{\bar{\rho}}\frac{\partial (\overline{w'T'}_a/\cos\alpha)}{\partial z} = \frac{1}{\cos\alpha}\frac{1}{\bar{\rho}}\frac{\partial \overline{w'T'}_a}{\partial z} + \overline{w'T'}_a\left(\frac{\sin\alpha}{\cos^2\alpha}\right)\frac{d\alpha}{dz} \quad (15)$$~~

Equation (~~15~~21) indicates that the altitude dependent α raises a term $\overline{w'T'}_a(\sin\alpha/\cos^2\alpha)\,d\alpha/dz$ as compared to the altitude independent α. This term complicates the estimation of uncertainties caused by α.

Generally, the uncertainty associated with the ~~uncertainties of the~~ angle α leads to a systematic underestimation of ~~underestimates the amplitude of the~~ GW-induced vertical velocity and heat flux by a factor of $1/\cos\alpha$. ~~If the angle~~When the angle α is independent of altitude, the ~~derived~~ GW-induced ~~parameters~~heat fluxes derived from along-track observations are ~~about~~ approximately $\cos\alpha$ times ~~of~~ their true ~~parameters~~values. Specifically, for $\alpha = 20°, 40°, 60°, 80°$, the values of $\cos\alpha$ are about 0.94, 0.77, 0.50, 0.17, respectively. However, ~~The m~~more complex scenarios ~~cases are that~~arise when ~~the angle~~ α ~~may change~~ varies between different~~from one~~ sampling profile ~~to another~~ or ,varies with altitude ~~and that the angle α may change with altitude~~. Notably, determining the actual horizontal propagation direction of GWs from SABER limb-viewing observation remains a challenging task~~However, the actual propagation direction is difficult to determine by SABER limb sampling~~.

Another source of uncertainty arises from the proportion (α_{down}) of downward-propagating GWs within the total GW population. Previous ground-based observational studies have

demonstrated significant variations in α_{down} across different geographic locations and seasons, with peak values reaching 50% and or higher (Chu et al., 2022; Gavrilov et al., 1996; Jandreau et al., 2026; Strelnikova et al., 2020; Vadas et al., 2018). Recently, Guarino et al. (2024) developed a novel GW parameterization describing vertical mixing by non-breaking GWs and implemented it into a chemistry climate model. In their scheme, they assume a fixed proportion ($\alpha_{down} = 33\%$) of downward-propagating GWs, independent of altitude, geographic location, or season. Their results showed that downward-propagating GWs produce non-negligible wave-induced vertical mixing and tracer flux in the MLT, which cannot be ignored in global chemistry-climate simulations. Both ground-based observations and models typically separate the upward- and downward-propagating GWs prior to heat fluxes and heating rates calculations. In contrast, our method retrieves global heat fluxes and heating rates from SABER temperature profiles at the cost of not distinguishing between upward- and downward-propagating GWs. Consequently, both upward- and downward-propagating GWs contribute to downward heat fluxes and cooling of the background atmosphere. This leads to an overestimation of absolute magnitudes of heat fluxes and heating rates.

The statistical correction of climatological heat fluxes and heating rates may rely on prior assumptions of wave directional distributions based on existing knowledge of wave sources and their propagation environment. For instance, independent observations by lidar, airglow imagers and GW-resolving model simulations can provide supplementary constrains on the directionality spectral of GWs. These complementary data can be utilized to calibrate the azimuthal weighting function and thereby reduce bias in climatological means. However, limitations arise due to inconsistencies in temporal-spatial sampling between different instruments, and discrepancies between model parameterizations and real atmospheric GW conditions. Future tomographic limb-imaging concepts observations can retrieve atmospheric parameters across the plane perpendicular to the line of sight from each limb scan. As a candidate mission of ESA's Earth Explorer 11, the CAIRT (Changing-Atmosphere Infra-Red Tomography) is a Fourier transform infrared limb imager and observes simultaneously from the middle troposphere to the lower thermosphere with a ~400 km-wide swath. Subsequent limb-images further enable the reconstruction of three-dimensional spatial distributions of atmospheric parameters. Such capabilities will open new avenues for investigating the propagation directions and associated impacts of GWs (Errera et al., 2026; Malavart et al., 2025).

4 Global and seasonal morphology of the derived parameters

The high spatial and temporal resolutions of lidar measurements provide reliable retrievals of heat fluxes and heating rates at ~80–100 km, with data collected over multiple ~~over several~~ stations. While ~~L~~lidar observations are mainly restricted to clear-sky nighttime conditions, thereby ~~and therefore have limited~~ limiting their temporal continuity. ~~However,~~Although the propagation directions of GWs cannot be retrieved from SABER observations, its continuous global observations together with the retrieval method developed in Section 2 provides an opportunity to investigate the global morphology of heat fluxes and heating rates. In this section, the year-to-year variations are neglected, all profiles from 2002 to 2025 are composited to form a composite year dataset. This enhances the statistical confidence of derived quantiles (e.g., the mean and P90), particularly at high latitudes.

4.1 Variations of GW amplitudes

Figure 3 shows the month-altitude distributions of the mean and P90 values ~~of~~ for $|T'/\bar{T}|$ and $|w'|$ at high (75°N/S), middle (45°N/S), and low (15°N/S) latitudes. Overall, the month-altitude patterns of the mean and P90 fields ~~of~~ for $|T'/\bar{T}|$ and $|w'|$ are qualitatively analogous. The main difference is that the P90 magnitudes ~~of P90~~ are about twice ~~as large as their~~the corresponding mean values. At high latitudes, both statistical quantiles exhibit altitude-dependent seasonal variations. The $|T'/\bar{T}|$ field is dominated by annual oscillations, with winter~~time~~ maxima in each hemisphere below ~75 km and transitioning~~translating~~ to summer~~time~~ maxima above ~85 km. A weak transition layer exists~~Seasonal variations are very weak~~ at ~75–85 km~~–~~, with minimal seasonal variation observed~~transition layer~~. Above ~85 km, a weak winter peak~~s~~ emerge at 75°S, whereas no ~~such~~ comparable feature is evident at 75° N. At middle latitudes, the seasonal variations ~~are similar to~~resemble those at high latitudes. The main difference is that the hemispheric winter maxima shift downward from ~75 km at high latitudes to ~70 km at middle latitudes. In addition, ~~the~~ semiannual oscillations are stronger at ~70–80 km ~~are stronger than those~~ compared to ~~seen~~ their~~at~~ high latitude counterparts~~s~~. By comparison, ~~the~~ seasonal oscillations at low latitudes are far weaker than their mid- and high-latitude counterparts.

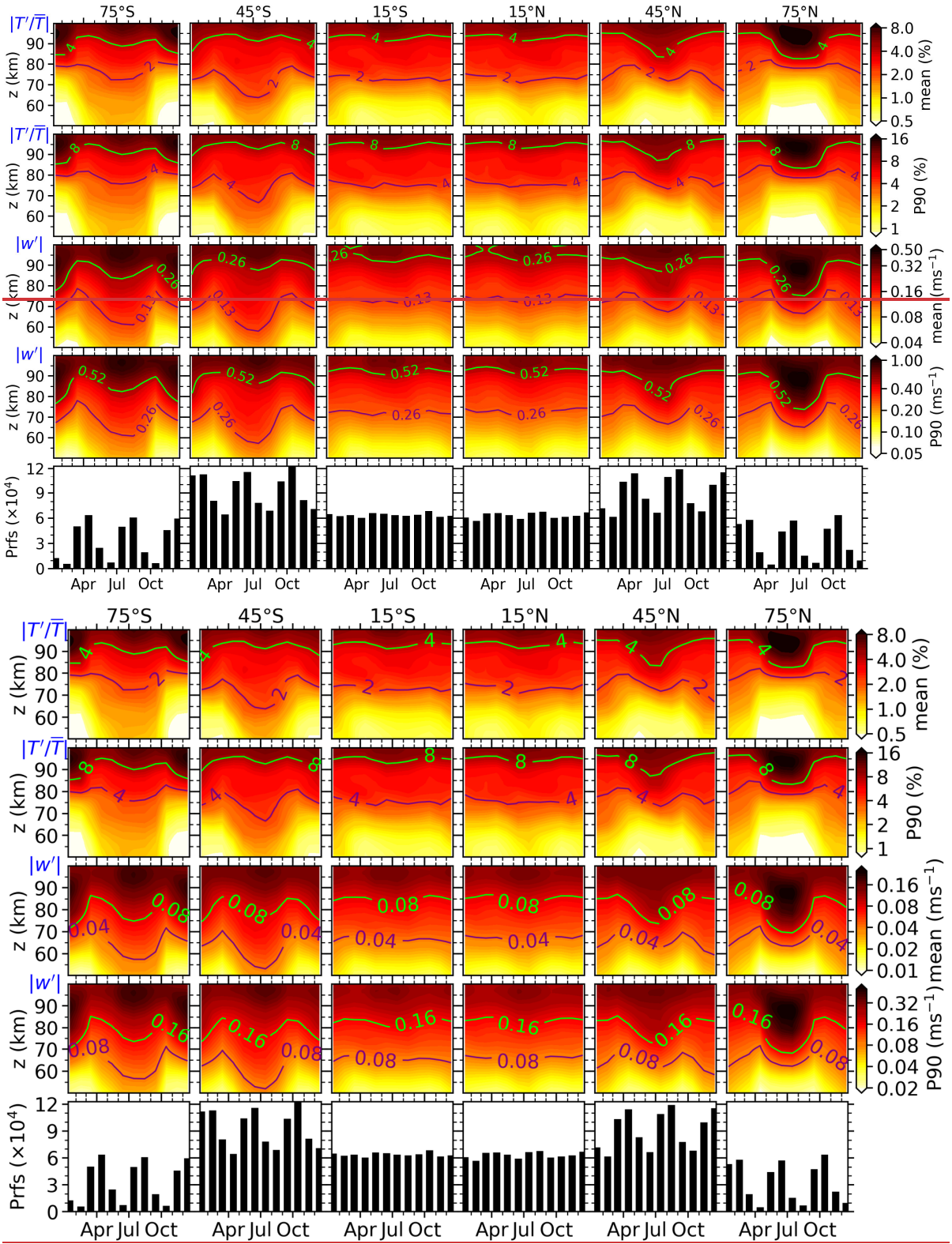


Figure 3. Month-altitude distributions of monthly-mean and monthly-P90 ~~of~~ for $|T'/\bar{T}|$ (1st and 2nd rows) and $|w'|$ (3rd and 4th rows) at high (75°N/S), middle (45°N/S), and low (15°N/S) latitudes. Bottom row shows the numbers of profiles. Here, the month denotes the composite month derived over 2002–2025.

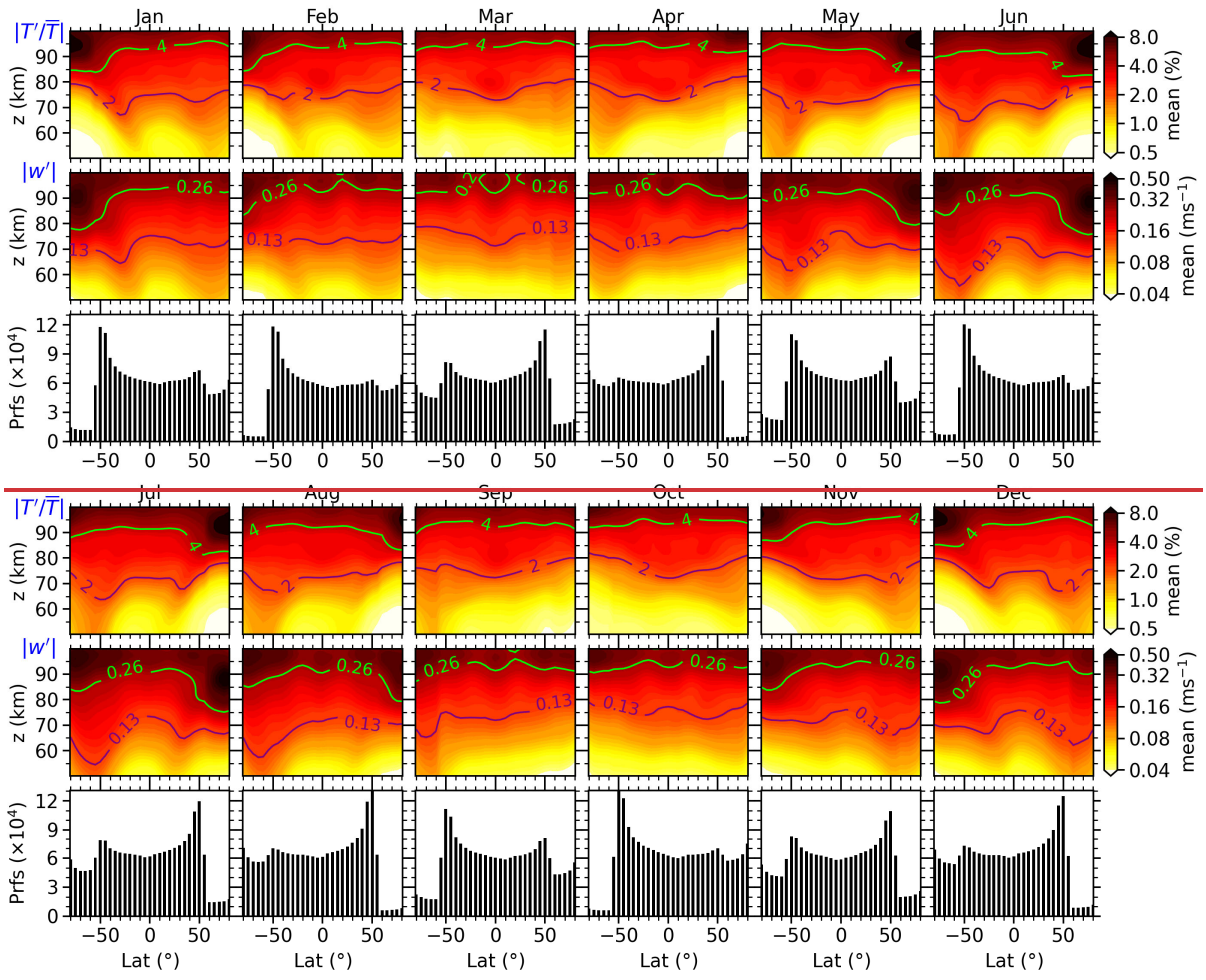
The mean and P90 of $|w'|$ exhibit altitude-dependent seasonal oscillations that are analogous to those observed for~~of~~ $|T'/\bar{T}|$. Two key distinctions exist between these two fields. First, the annual maxima of $|w'|$ in each hemisphere shift downward relative to $|T'/\bar{T}|$. The annual maxima of $|w'|$ occur~~s~~ near ~90 km, while the corresponding ~~maximum~~ maxima of $|T'/\bar{T}|$ ~~is~~ are located at ~ 95 km. Second, pronounced semiannual oscillations in $|w'|$ occur~~s~~ at ~60–75 km and across middle and high latitudes. These semiannual oscillations ~~have~~ reach their maxima in winter and summer months of each hemisphere. Notably, such summer semiannual maxima below 75 km that occur in $|w'|$ are absent in $|T'/\bar{T}|$. A plausible physical explanation ~~of~~ for ~~the summum maxima of $|w'|$ below 75 km~~this phenomenon is that w' is more sensitive to ~~the~~ high-frequency GWs (Eq~~uation 2~~. 3). In summer, convection is one of the dominant GW sources, emitting abundant high-frequency GWs with fast horizontal phase speeds. These GWs can propagate upward into the stratosphere and mesosphere and thus generate the summer maxima. The seasonal variations of $|T'/\bar{T}|$ and $|w'|$ are strongest at high latitudes, moderately strong~~er~~ at middle latitudes, and weak at low latitudes. These seasonal variations vary continuously across latitude bands and can be interpreted as a genuine physical feature, rather than an artifact arising from uneven monthly sampling profiles at high latitudes.

The latitude-altitude distributions of the mean~~s of~~ $|T'/\bar{T}|$ show that their maxima ~~are~~ occur at high latitudes around summer months above ~85 km (~~Figure~~ Fig. 4). Specifically, in January, February, November, and December, their maxima ~~are at latitudes higher than~~occur poleward of 50°S. In May, June, July, and August, their maxima ~~are at latitudes higher than~~occur poleward of 50°N. Below ~75 km, the mean~~s of~~ $|T'/\bar{T}|$ ~~reach their maxima~~ peaks around 60°±20° in the winter hemisphere ~~and weaker~~with secondary peaks around 20°±10° in the summer hemisphere. ~~Moreover, the~~These pattern~~s~~ suggest~~s~~ that the high-latitude summer maxima ~~at high latitudes~~ above ~85 km ~~is~~ originate~~s~~ from low- and mid-latitudes (i.e., 10°–30° of the summer hemisphere) ~~at~~ near ~50 km.

The latitude-altitude distributions of the mean~~s of~~ $|w'|$ exhibit a similar pattern ~~as~~ to those of $|T'/\bar{T}|$ in each month. The differences can be attributed to two aspects. First, the heights at which ~~of~~ high-latitude summer maxima occur for~~at high latitudes of~~ $|w'|$ are ~5 km lower than those ~~of~~ for $|T'/\bar{T}|$ in the same month. For ~~example~~instance, in January and ~~at latitudes higher than~~poleward of 50°S, the maxima of $|w'|$ and $|T'/\bar{T}|$ ~~are~~ occur at ~90 km and ~95 km, respectively. Second, the mean~~s of~~ $|w'|$ have peaks at high latitudes of winter hemisphere above

~85 km, which are weaker and at a lower ~~height~~ altitudes ~~as compared~~relative to their summer ~~maxima~~counterparts.

Figures 3 and 4 reveal that the winter maxima of $|w'|$ above ~85 km over ~~the~~ southern high latitudes exceed their northern counterparts~~.~~, ~~This indicates the~~indicating pronounced hemispheric asymmetry in $|w'|$. The mean values of $|T'/\bar{T}|$ exhibit similar hemispheric asymmetry, although with a weaker ~~the~~ interhemispheric contrast ~~is less pronounced compared~~relative to that of $|w'|$. ~~Also, a~~Above ~85 km, the summer maxima of both $|T'/\bar{T}|$ and $|w'|$ at northern high latitudes are larger than their southern counterparts. Furthermore, the summer peaks of both $|T'/\bar{T}|$ and $|w'|$ are stronger than ~~their~~ winter ~~counterparts~~ peaks over high latitudes. Collectively, ~~T~~these features demonstrate clear interhemispheric and seasonal asymmetries in ~~the~~ GW amplitudes at high latitudes. However, such interhemispheric and seasonal asymmetries of the GW amplitudes are ~~less distinct~~much weaker at low latitudes.



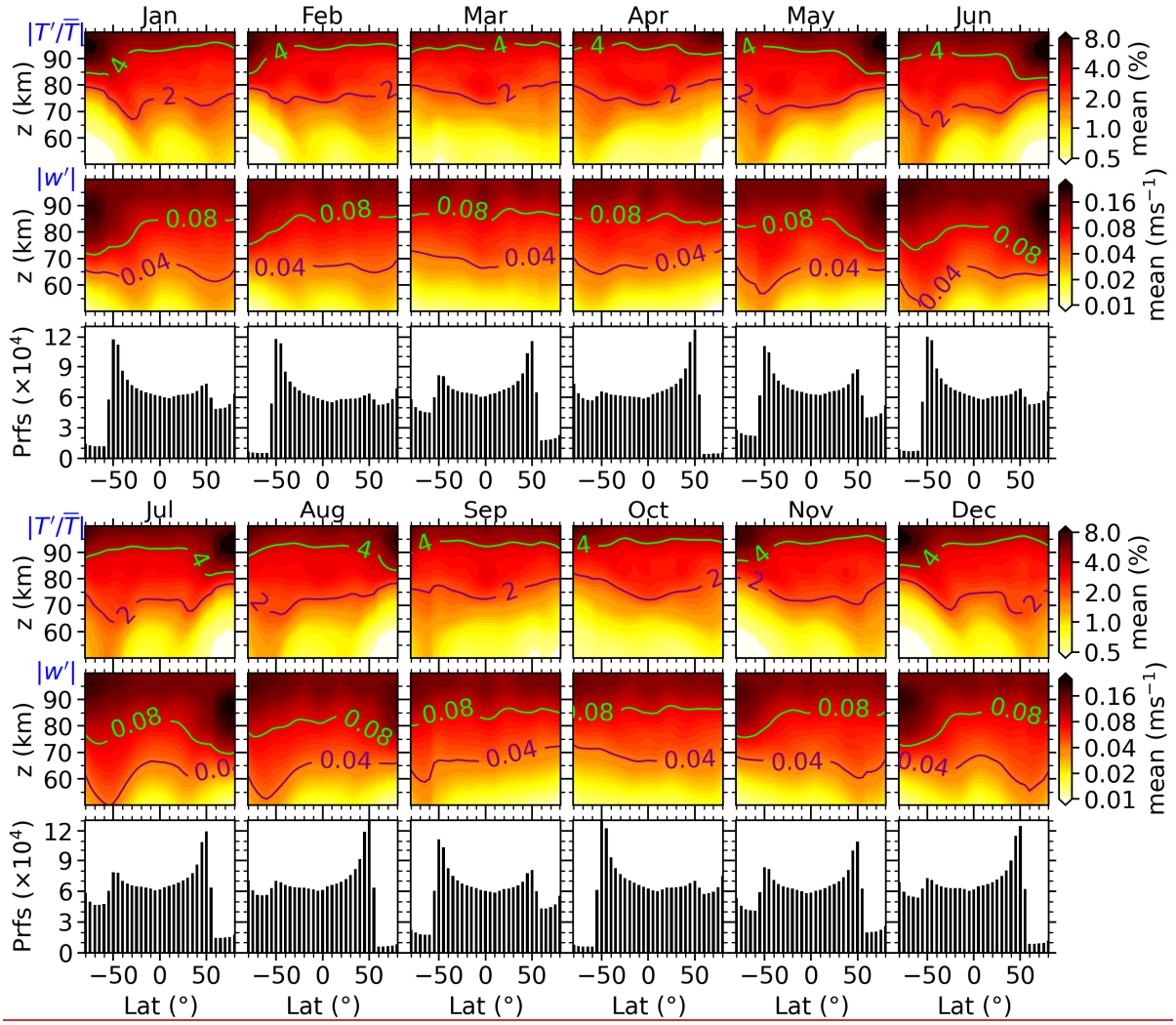


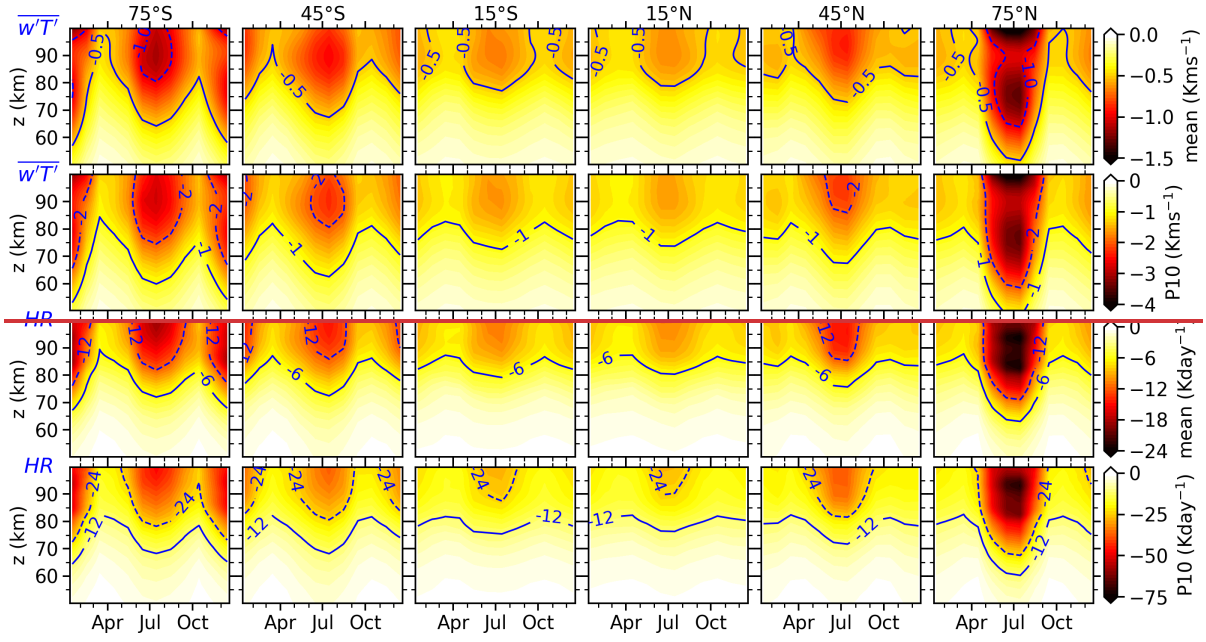
Figure 4. Latitude-altitude distributions of monthly-mean of $|T'/\bar{T}|$ (1st and 4th rows) and $|w'|$ (2nd and ~~4th~~-5th rows) in each month. The numbers of profiles are shown in the 3rd and 6th rows.

~~Although t~~The number of sampled profiles poleward of 55°S is substantially lower in January and February ~~compared with~~relative November and December. This uneven sampling distribution ~~of sampling profiles~~ at high latitudes ~~is caused by~~arises from ~~the~~ SABER's yaw-maneuver ~~of SABER~~observation mode. ~~However~~Nevertheless, the corresponding latitude-altitude patterns of the means $|T'/\bar{T}|$ and $|w'|$ remain consistent across these four months. A ~~minor distinction~~subtle difference is that the latitudinal gradients of the means ~~of~~ $|T'/\bar{T}|$ are steeper around 55°S in January and February than in November and December. Likewise, May and June exhibit latitude–altitude patterns and ~~similarly~~ intensified ~~meridional~~ latitudinal gradients around 55°~~S~~ N ~~as~~ similar to~~observed in~~ July and August. These results further confirm that uneven sampling ~~counts~~ poleward of 55° in both hemispheres does not fundamentally influence the physical characteristics

governing the seasonal and latitudinal variability of $|T'/\bar{T}|$ and $|w'|$, ~~yet they~~although it introduces sharper ~~meridional~~ latitudinal transitions around 55°N/S.

4.2 Variations of heat flux and heating rate

Figure 5 shows the statistical quantiles (mean and P90) of heat flux ($\overline{w'T'}$) and heating rate (HR) as a function of month ~~and~~ altitude ~~at~~ across six latitude bands, ~~ranging from~~spanning high to low latitudes ~~of~~ in each hemisphere. Generally, the mean~~s~~ and P90 values ~~of~~ for heat flux exhibit similar month-altitude patterns. The magnitudes of the P90 for heat flux ~~of heat flux~~ are approximately ~~two times~~twice ~~larger than~~ those of the corresponding means. The mean~~s~~ and P90 of heating rate behave similarly to those ~~are in a similar situation to~~ of heat flux. For illustration purposes only, ~~T~~the P90 of heat flux and heating rate are shown here ~~is only~~ to ~~illustrate~~ highlighting their ~~large~~ substantial variabilities and negative skewness at each ~~height~~altitude. Subsequent~~The following~~ analysis focus~~es~~ on the mean~~s of~~ values of heat flux and heating rate.



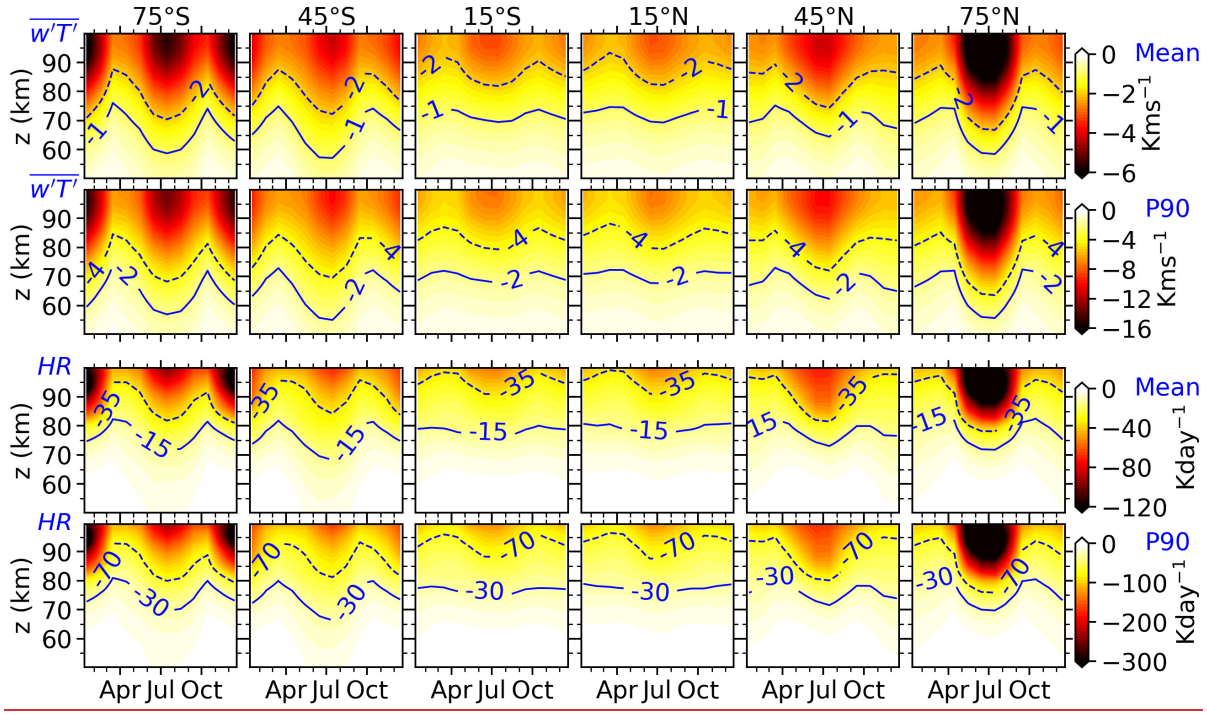
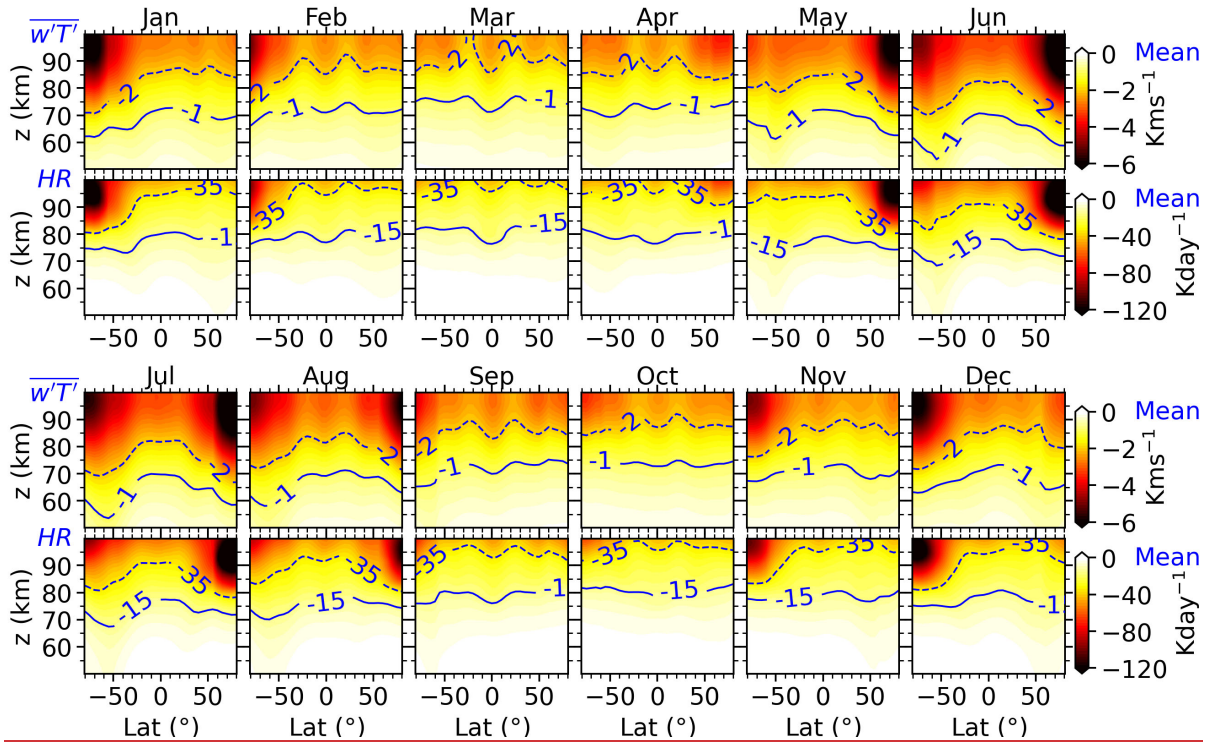


Figure 5. Month-altitude distributions of monthly-mean and montly-P90 of heat flux (1st and 2nd rows) and heating rate (3rd and 4th rows) at high (75°N/S), middle (45°N/S), and low (15°N/S) latitudes.

The heat flux shown in Figure 5 exhibits a clear semiannual oscillation at 75°S with peaks occurring in winter and summer. Notably, the December peak around is more pronounced than that ~~and annual oscillation at 75°N. The peaks appear in winter and summer at 75°S and in summer at 75°N. While the peaks around December is stronger than those~~ around July. In contrast at 75°N, the heat flux exhibits an annual oscillation with peak in summer. At middle latitudes ~~of~~ in both hemispheres, ~~the~~ semiannual oscillations are superimposed ~~by~~ on ~~semi~~annual oscillations, with stronger peaks observed around July. At low latitudes ~~of~~ in both hemispheres, ~~the~~ semiannual oscillations ~~are in the dominant position~~dominate and exhibit ~~with~~ comparable peak magnitudes in summer and winter. We ~~note that the~~observe an increase in peak magnitudes ~~in summer of both hemispheres increase with the as~~increasing latitude~~s~~ increases during summer months of both hemispheres. These ~~features~~ patterns of annual and semiannual oscillations can also be seen in heating rates.

However, both heat flux and heating rate exhibit interhemispheric and seasonal asymmetries. These asymmetries can be summarized as follows. First, the summer maxima of heat flux are ~~-~~approximately ~~-~~1.56 Kms^{-1} at 75°N, which are larger than the corresponding values of ~~-~~approximately ~~-~~15.0 Kms^{-1} at 75°S. The winter maxima are approximately ~~-~~0.83 Kms^{-1} at 75°N,

which are less than the corresponding values of approximately ~~−~~1.26 Kms^{-1} at 75°S. Second~~, at 75°N, the summer maxima occur at altitudes of ~75 km and ~100 km, separated by a valley at ~88 km. This vertical valley structure is less pronounced at 75°S. We note that the vertical valley structure of summer heating rate maxima is less pronounced as compared to that of heat flux at 75°N. Third~~, according to the contour lines (~~−0.5~~2 Kms^{-1} for heat flux and ~~−12~~ 35 Kday^{-1} for heating rate), the summer maxima extend over a wider altitude range at 75°N than at 75°S. ~~Fourth~~Third, the heat flux and heating rate at 75°S has equivalent magnitudes in summer and winter above 80 km. In contrast, the heat flux and heating rate at 75°N is much larger in summer than in winter. These features demonstrate~~show the~~ interhemispheric asymmetry in both the magnitude and vertical structure of the summer maxima ~~of~~ for heat flux and heating rate.



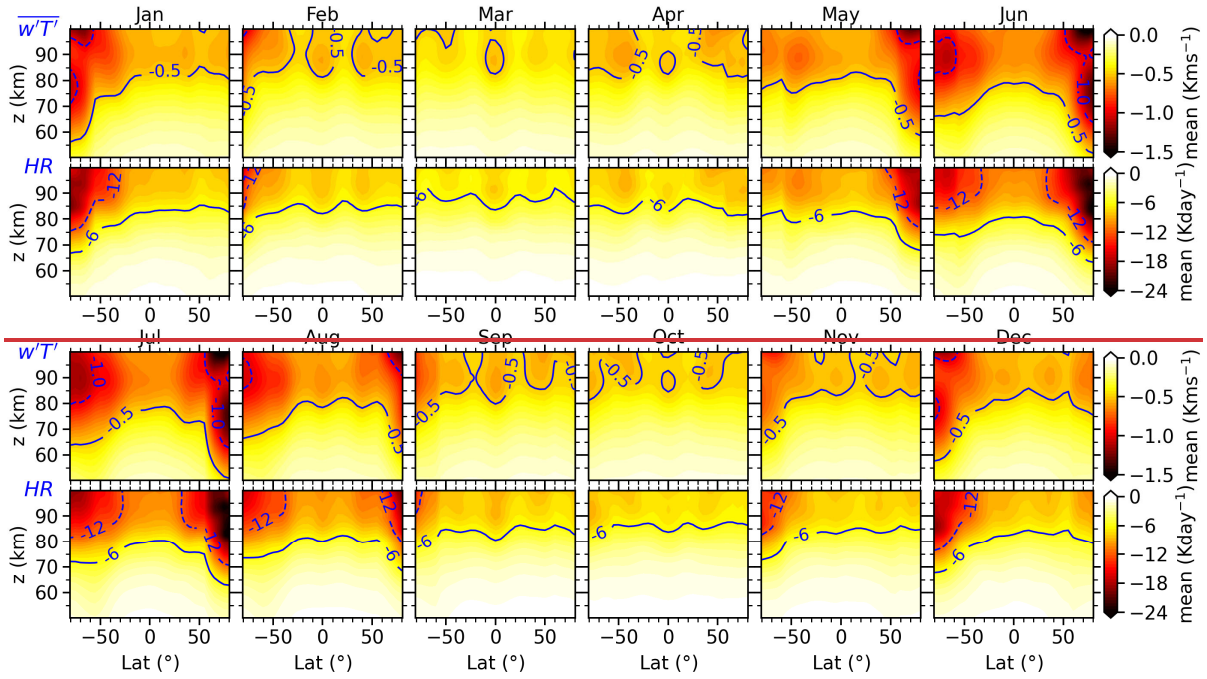


Figure 6. Latitude-altitude distributions of monthly-mean heat flux (1st and 3rd rows) and heating rate (2nd and 4th rows).

Figure 6 shows the latitude-altitude distributions of heat flux and heating rate to characterize their latitudinal variations ~~in~~ for each month. During November–February, the heat flux and heating rate reach their peaks at southern high latitudes. In contrast, during May–August, the heat flux and heating rate exhibit dual peak structures at high latitudes in both hemispheres. Additionally, the substantially larger magnitudes occur at northern high latitudes. Combined with the results in ~~Figure~~ Fig. 5, these patterns demonstrate clear interhemispheric and seasonal asymmetries. The summer (May–August) high-latitude peaks of heat flux and heating rate in the Northern Hemisphere feature larger amplitudes~~. They also span~~ and a broader vertical extent. By comparison, the corresponding high-latitude peaks in the Southern Hemisphere's summer (November–February) and winter (May–August) are weaker. During equinoctial months (March, April, September, and October), weak peaks of heat flux and heating rate emerge around the equator and 50°N/S.

5 Discussion

Based on the perturbed thermodynamic equation for~~linear GW dispersion and polarization relation in~~ a dissipative, partially compressible atmosphere, we derive ~~the~~ global GW-induced heat fluxes and heating rates ~~are derived~~ from SABER temperature measurements without distinguishing between upward- and downward-propagating GWs. The ~~main~~ primary assumption

is that ~~the~~ GWs ~~propagating~~ propagate ~~in the~~ along the SABER orbit~~-~~ track ~~direction of SABER orbit~~. To quantify ~~The u~~uncertainties, ~~are quantified by introducing~~ an angle α~~, which denotes the deviation~~ is introduced to represent the departure of the ~~actual~~ true GW ~~propagating~~ propagation direction ~~relative to~~from the along-track direction. In the simple case ~~that~~ where the angle α ~~does not change with~~is altitude-independent, we find that the retrieved heat fluxes and heating rates are systematically underestimated by a factor of $\cos\alpha$. Our results indicate that~~Overall,~~ the monthly mean heat fluxes and heating rates are ~~of ~~approximately $-$~~0.7~~3 Kms^{-1} and ~~~~$-$~~12~~ 40 Kday^{-1}, with standard deviations of ~~1.1~~5 Kms^{-1} and ~~20~~ 80 Kday^{-1}, respectively. ~~They~~ These values are ~~~0.3–0.5 times~~comparable to ~~the~~ lidar ~~derived value~~ retrievals and ~~are ~0.5 times of~~ theoretical predictions, suggesting the reliability of the derived heat fluxes and heating rates.

Despite these inherent uncertainties, the GW-induced heat fluxes and heating rates presented in this study offer distinct advantages, including global spatial coverage and continuous temporal coverage ~~spanning~~ from 2002 to 2025. The derived heat fluxes and heating rates ~~derived here~~ are strongly correlated to the GW amplitudes, exhibiting latitudinal dependence in both annual and semiannual oscillation, as well as interhemispheric and seasonal asymmetries in their peak magnitudes. The month-altitude patterns of GW amplitudes and the corresponding GW-induced heat fluxes and heating rates are comparable ~~with~~ to nighttime lidar observations at SOR (35°N) reported by Gardner and Liu (2007). Their lidar results showed that the GW temperature variance (T'^2) reaches its maxima in winter and summer at altitudes above 100 km and ~85–95 km, with winter peaks larger than summer ones. In contrast, vertical wind variance (w'^2) is dominated by annual oscillations and ~~is~~ maximized in summer. The summer peaks occur near 85 km and 92 km, which are lower in altitude than the corresponding ~~peaks of~~ temperature variance peaks. These seasonal and altitudinal features support the results presented in ~~Figure~~ Fig. 3. The SOR lidar-derived heat fluxes and heating rates exhibit negative peaks near 90 km in both winter and summer, with winter peaks being more negative than their summer counterparts. Gardner and Liu (2007) suggested that variations in heat fluxes and heating rates are closely related to GW ~~intensity~~amplitude. The ~~GW-induced heat flux and heating rate~~results derived here support this conclusion. By integrating the comparisons from Section 3.2 with those discussed here, we emphasize the consistent agreement between our findings and previous lidar measurements in terms of both magnitude and spatial-temporal patterns.

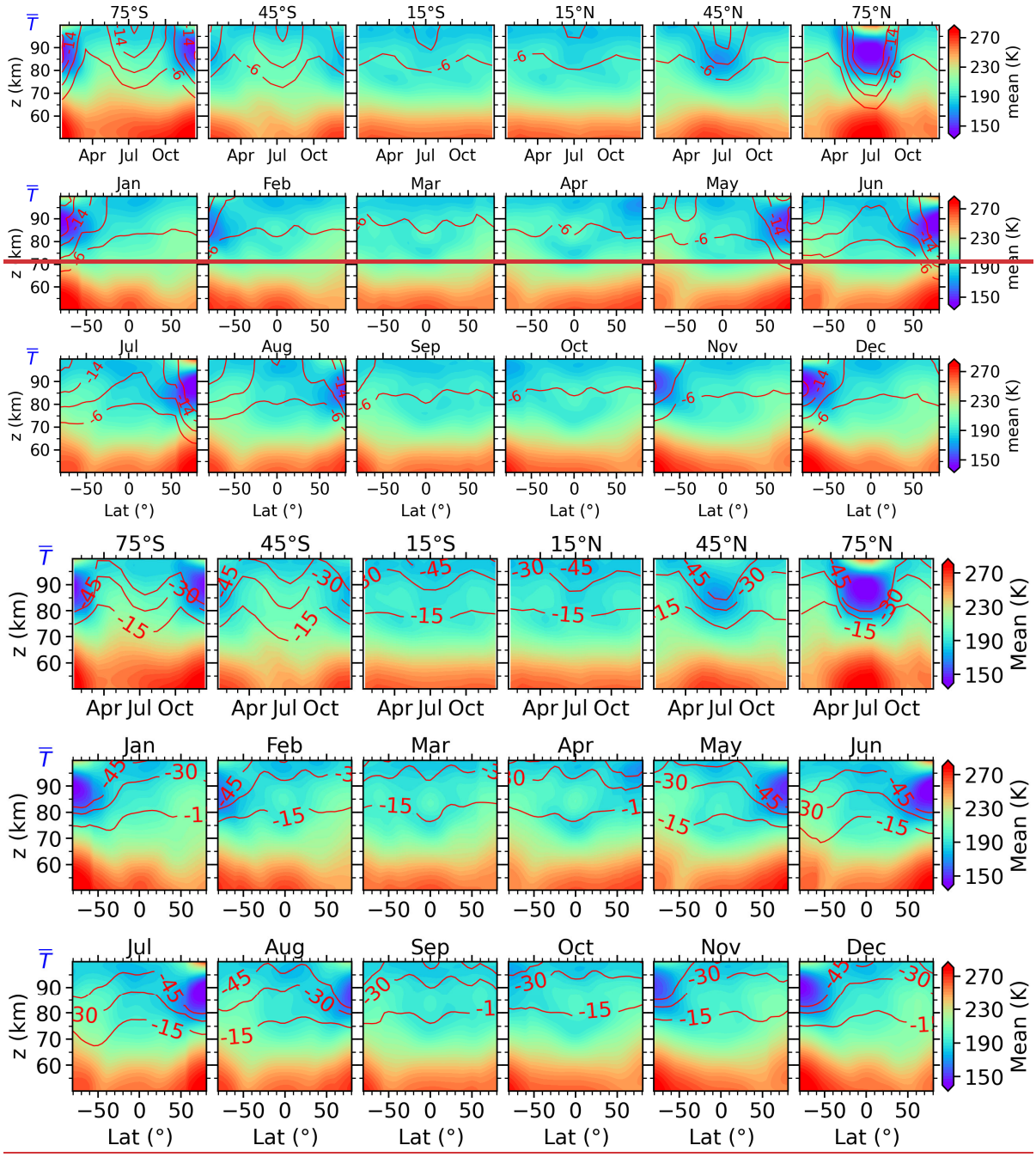


Figure 7. Monthly-mean of background temperature as a function of month and ~~latitude~~ altitude (1st row~~s~~) and as a function of latitude and altitude (2nd and 3rd rows). The heating rate is overplotted by contour lines with interval of ~~4~~ 15 Kday^{-1}.

Nevertheless, several discrepancies exist between our results and those obtained from the lidar observations~~the two results~~. First, ~~unlike the lidar observations, there is no the summer maximum of T'^2 above 100 km in Figure 3. This is because of wavelet edge effects during GW extraction from SABER temperature measurements. We do not analyze GWs extracted from~~

~~SABER temperature above 100 km.~~ ~~Second,~~ the lidar-observed T'^2 valley near 95 km observed by the lidar is absent in our results. This discrepancy can be attributed to oscillations of T'^2 ~~oscillates~~ at twice the wavenumber and its variation~~varies~~ with the instantaneous phase of the perturbation. The amplitude in ~~Equation~~ Eq. (~~1~~2) ~~is~~ calculated from the Hilbert transform~~, which~~ removes the dependence on the instantaneous phase~~, in T'^2~~ ~~and~~ represent~~s~~ing the slowly varying envelope of the perturbation. ~~Third~~Second, the month-altitude patterns of lidar-derived heat fluxes and heating rates are more complex ~~than those derived here~~compared to those derived in our study. ~~Fourth~~Third, positive values of heat fluxes and heating rates retrieved from lidar observations are not fully reproduced here. The last two discrepancies are likely attributed to (1)~~the~~ distinct GW spectral ranges resolved by lidar and SABER, and (2) unresolved upward- and downward-propagating GWs from SABER temperature measurements.

Now, we discuss ~~the relations of~~ global morphology ~~between~~ of heating rates and background temperatures, as well as their relationships. Figure 7 shows the distributions of monthly-mean background temperature as ~~a~~ functions of month ~~and~~ -altitude and ~~as a function of~~ latitude ~~and~~ -altitude. Comparisons between ~~the~~ GW-induced heating rates and background temperatures ~~show~~ reveal that the cold summer mesopause coincides well with the enhanced absolute magnitudes of heating rates at mid- and high-latitude. Furthermore, the summer mesopause is colder at 75°N and 45°N ~~than that at~~compared to 75°S and 45°S, respectively. This feature is consistent with ~~enhanced~~ larger absolute magnitudes of summer heating rates over northern mid- and high-latitude relative to their southern counterparts. At low latitudes, the slightly ~~the stronger~~larger absolute magnitudes of heating rates in summer ~~is~~ are consistent with ~~the~~ a slightly colder mesosphere relative to other seasons. The relationships among GW~~s'~~ strength, mesopause height and temperature at high latitudes have been studied ~~through~~ using global models with different ~~GW~~ parameterization schemes and ~~GW~~ sources for GWs (Berger and Von Zahn, 1999; Garcia and Solomon, 1985; Siskind et al., 2003). The summer mesopause structures exhibit ~~large~~ significant discrepancies among ~~different~~ these models. A general conclusion is that adiabatic heating/cooling ~~caused~~ induced by ~~the~~ meridional circulation~~, which is~~ are highly sensitive to GW forcing. This highlights the necessity~~illustrates the importance~~ of quantifying GW amplitudes~~the strengths of GWs~~ and their associated heating/cooling rates~~.~~, particularly at high latitudes where they play a crucial role in modulating the mesopause height and temperature.

The energy balance in the MLT is controlled by many dynamical and chemical processes ~~in the MLT~~. ~~The s~~Solar heating and chemical heating contribute~~are~~ ~10 K~~/~~day^{-1} and ~10−15 K~~/~~day^{-1}, respectively (Mlynczak and Solomon, 1993; Smith, 2004; Wu et al., 2026; Xu et al., 2007).

Radiative cooling ~~caused by~~due to CO_2 is about −15 K~~/~~day^{-1} (Mlynczak et al., 2024; Mlynczak et al., 2018). The adiabatic heating and cooling rates caused by meridional circulation reach peaks about 15 K~~/~~day^{-1} in the winter polar MLT and −15 K~~/~~day^{-1} in the summer polar MLT, respectively (Smith, 2004; Yue and Wang, 2025). In comparison to these processes~~Compared to the above-mentioned heating/cooling rates~~, ~~the~~ GW-induced heating rates are ~~of~~ on the order of ~~10~~ 40 K~~/~~day^{-1}, ~~which are~~This value is ~~in quantitative agreement with the~~larger than adiabatic cooling rates. This quantitative comparison illustrates the importance role of non-breaking GWs in heating/cooling the local atmosphere and the energy balance in the MLT~~e~~.

We note that the enhanced absolute magnitudes of heating rates extend from about 70 km to 100 km, whereas, ~~the heights of~~ mesopause heights are mainly ~~at~~ around ~85−95 km at high latitudes ~~of~~ in the summer hemisphere~~s~~. This indicates that the enhanced absolute magnitudes of heating rates above the mesopause are not ~~the only factor of determining~~solely responsible for shaping the thermal structure of the lower thermosphere. In fact, the spatial and temporal variations ~~of~~ in the thermal structures are ~~determined~~ influenced by many heating/cooling ~~sources~~mechanisms. Specifically, although the diffusive and O_2 heating rates are very small, they increase with altitude ~~and reach~~to peaks of ~10−20 K~~/~~day^{-1} at ~100−110 km (Smith, 2004). Moreover, the narrow warm region above the cold summer mesopause has also been revealed by Yue and Wang (2025). This may be partially explained by the decreasing adiabatic cooling rate above summer mesopause and auroral heating (Smith, 2004; Yue and Wang, 2025).

6 Conclusions

The importance of heat flux~~es~~ and heating rate~~s~~ induced by non-breaking GWs ~~have~~ has been quantified by ground-based lidar observations. However, ~~T~~the~~ir~~ global distributions of these quantities ~~are~~ remain unknown ~~yet. This is~~ due to ~~the unavailable~~lack of vertical wind measurement~~s~~. To partially ~~overcome~~ address this limitation, we derive the GW-induced vertical wind ~~via the~~using the perturbation thermodynamic equation~~linear GW theory~~ in a dissipative, partially compressible atmosphere and ~~from the~~ temperature profiles measured by SABER during 2002–2025. Based on these derived vertical winds, ~~Then~~ we then calculate the global ~~the~~ GW-induced heat flux~~es~~ and heating rate~~s are also derived~~. The main conclusions are summarized as below.

The GW-induced parameters ($|T'/\bar{T}|$, $|w'|$, heat flux, and heating rate) at 35°N are analyzed and compared with lidar observations. The derived heat fluxes are ~~mainly~~ downward and cool the background atmosphere, ~~which~~ with peak magnitudes occurring around 90 km. At 80–100 km, the

The mean values of heat fluxes and heating rates have mean values ofare ~−0.73 Kms^{-1} and ~−12Kday40 $Kday^{-1}$, respectively. with Their standard deviations of ~1.15 Kms^{-1} and ~20–80 $Kday^{-1}$ at 80–100 km, respectively. The derived heating rates are comparable to those observed by lidars and almost equivalent tolarger than the adiabatic cooling rates reported beforepreviously. It is important to note that these parameters are derived from the observed vertical variation of multiple monochromatic wave amplitude envelopes, regardless of their upward or downward propagation directions. This unresolved vertical directional ambiguity will overestimate the GW-induced heat fluxes and heating rates.

The global spatial and temporal distributions of the GW-induced parameters are studied in a composite year derived over 2002–2025. The aAnnual oscillations are dominant in $|T'/\bar{T}|$ and $|w'|$ at high latitudes of within summer hemispheres. The annual, with annual maxima of $|T'/\bar{T}|$ and $|w'|$ are locatedoccurring at ~ 95 km and ~90 km, respectively. In contrast, heat fluxes and heating rates exhibit clear semiannual oscillations, with peaks in both winter and summer hemispheres. Moreover, GW-induced parameters show notable interhemispheric and seasonal asymmetries, especially particularly evident at high latitudes. Such These interhemispheric asymmetryies supports the colder summer mesopause at northern high latitudes as compared to that at southern high latitudes.

Although our retrievedThe magnitudes of heat fluxes and heating rates are ~0.3–0.5 times theagree with lidar-derived values and are ~0.5 times of the theoretical valuespredictions, multiple competing bias sources affect the results. This discrepancy is mainly attributed to uncertainties of wave propagation direction. Underestimation arises from uncertainties in the horizontal propagation direction of GWs, which can reduce the retrieved heat fluxes and heating rates by a factor of $\cos\alpha$ if α is independent of altitude. The uncertainty of GW propagation direction underestimates heat fluxes and heating rates by a factor of $\cos\alpha$. Moreover, SABER's the observational filter and limited detectable wavelength range preferentially capture wavelengths observable by SABER are favor waves with long horizontal wavelengths., leading to the underestimation of Thus, the unobserved waves with sshort-wavelength wavess, which can that also contribute to GW heat transportheat fluxes and heating, are omitted and induce an underestimation. Conversely, overestimation arises from the unresolved separation between upward- and downward-propagating GWs. Future tomographic limb-imaging observations (e.g., CAIRT) and high high-resolution model simulations, can provide three-dimensional atmospheric parameters and overcome these limitations.

Data availability

All SABER data can be accessed from Space Physics Data Facility, Goddard Space Flight Center (https://spdf.gsfc.nasa.gov/pub/data/timed/saber/, last access: March 2026). Outputs of the method are available from the corresponding author upon request.

Author contributions

XL developed the conceptualization, formal analysis and drafted the manuscript. JX and JY provided supervision, discussion and validation. QL, ZY, YL, LV, and JM provided suggestions and revisions and helpful discussion.

Competing interests

The authors declare that they have no conflict of interest.

Acknowledgments

This work was supported by the National Natural Science Foundation of China (42574216, 42404170), the Project of Stable Support for Youth Team in Basic Research Field of Chinese Academy of Sciences (grant no. YSBR-018), This work was also supported by the Specialized Research Fund for State Key Laboratory of Solar Activity and Space Weather. JM thanks the Brazilian Ministry of Science, Technology and Innovation (MCTI), National Council for Scientific and Technological Development (CNPq) Grant 305041/2024-0.

References

Alexander, M. J., Gille, J., Cavanaugh, C., Coffey, M., Craig, C., Eden, T., Francis, G., Halvorson, C., Hannigan, J., Khosravi, R., Kinnison, D., Lee, H., Massie, S., Nardi, B., Barnett, J., Hepplewhite, C., Lambert, A., and Dean, V.: Global estimates of gravity wave momentum flux from High Resolution Dynamics Limb Sounder observations, J. Geophys. Res.: Atmos., 113, https://doi.org/10.1029/2007jd008807, 2008.

Becker, E. and Vadas, S. L.: Secondary gravity waves in the winter mesosphere: results from a high-resolution global circulation model, J. Geophys. Res.: Atmos., 123, 2605–2627, https://doi.org/10.1002/2017jd027460, 2018.

Berger, U. and von Zahn, U.: The two-level structure of the mesopause: A model study, J. Geophys. Res.: Atmos., 104, 22083–22093, https://doi.org/10.1029/1999jd900389, 1999.

Chu, X., Gardner, C. S., Li, X., and Lin, C. Y. T.: Vertical transport of sensible heat and meteoric Na by the complete temporal spectrum of gravity waves in the MLT above McMurdo (77.84°S, 166.67°E), Antarctica, J. Geophys. Res.: Atmos., 127, https://doi.org/10.1029/2021jd035728, 2022.

Dawkins, E. C. M., Feofilov, A., Rezac, L., Kutepov, A. A., Janches, D., Höffner, J., Chu, X., Lu, X., Mlynczak, M. G., and Russell III, J. M.: Validation of SABER v2.0 operational temperature data with ground-based lidars in the mesosphere-lower thermosphere region (75–105 km), J. Geophys. Res.: Atmos., 123, 9916–9934, https://doi.org/10.1029/2018jd028742, 2018.

Ern, M., Preusse, P., Alexander, M. J., and Warner, C. D.: Absolute values of gravity wave momentum flux derived from satellite data, J. Geophys. Res.: Atmos., 109, https://doi.org/10.1029/2004jd004752, 2004.

Errera, Q., Op de beeck, M., Bender, S., Flemming, J., Funke, B., Hoffmann, A., Höpfner, M., Livesey, N., Poli, G., Pieroux, D., Raspollini, P., and Sinnhuber, B.-M.: On the capability of the Changing Atmosphere Infra-Red Tomography explorer (CAIRT) candidate mission to constrain O3 and H2O in the upper troposphere and lower stratosphere, Atmos. Meas. Tech., 19, 2601–2620, https://doi.org/10.5194/amt-19-2601-2026, 2026.

Esplin, R., Mlynczak, M. G., Russell III, J. M., and Gordley, L.: Sounding of the Atmosphere Using Broadband Emission Radiometry (SABER): instrument and science measurement description, Earth Space Sci., 10, https://doi.org/10.1029/2023ea002999, 2023.

Fritts, D. C.: Gravity wave saturation in the middle atmosphere: A review of theory and observations, Rev. Geophys., 22, 275-308, https://doi.org/10.1029/RG022i003p00275, 1984.

Fritts, D. C. and Alexander, M. J.: Gravity wave dynamics and effects in the middle atmosphere, Rev. Geophys., 41, https://doi.org/10.1029/2001rg000106, 2003.

Garcia, R. R. and Solomon, S.: The effect of breaking gravity waves on the dynamics and chemical composition of the mesosphere and lower thermosphere, J. Geophys. Res.: Atmos., 90, 3850–3868, https://doi.org/10.1029/JD090iD02p03850, 1985.

Gardner, C. S.: Role of wave-induced diffusion and energy flux in the vertical transport of atmospheric constituents in the mesopause region, J. Geophys. Res.: Atmos., 123, 6581–6604, https://doi.org/10.1029/2018jd028359, 2018.

Gardner, C. S.: Impact of Atmospheric Compressibility and Stokes Drift on the Vertical Transport of Heat and Constituents by Gravity Waves, J. Geophys. Res.: Atmos., 129, https://doi.org/10.1029/2023jd040436, 2024.

Gardner, C. S. and Liu, A. Z.: Seasonal variations of the vertical fluxes of heat and horizontal momentum in the mesopause region at Starfire Optical Range, New Mexico, J. Geophys. Res.: Atmos., 112, https://doi.org/10.1029/2005jd006179, 2007.

Gardner, C. S. and Yang, W.: Measurements of the dynamical cooling rate associated with the vertical transport of heat by dissipating gravity waves in the mesopause region at the Starfire Optical Range, New Mexico, J. Geophys. Res.: Atmos., 103, 16909–16926, https://doi.org/https://doi.org/10.1029/98JD00683, 1998.

Gavrilov, N. M., Fukao, S., Nakamura, T., Tsuda, T., Yamanaka, M. D., and Yamamoto, M.: Statistical analysis of gravity waves observed with the middle and upper atmosphere radar in the middle atmosphere: 1. Method and general characteristics, J. Geophys. Res.: Atmos., 101, 29511–29521, https://doi.org/10.1029/96jd01447, 1996.

Geller, M. A. and Gong, J.: Gravity wave kinetic, potential, and vertical fluctuation energies as indicators of different frequency gravity waves, J. Geophys. Res.: Atmos., 115, https://doi.org/10.1029/2009jd012266, 2010.

Guarino, M. V., Gardner, C. S., Feng, W., Funke, B., García-Comas, M., López-Puertas, M., Kupilas, M. M., Marsh, D. R., and Plane, J. M. C.: A novel gravity wave transport parametrization for global chemistry climate models: description and validation, Journal of Advances in Modeling Earth Systems, 16, https://doi.org/10.1029/2023ms003938, 2024.

Guo, Y. and Liu, A. Z.: Seasonal variation of vertical heat and energy fluxes due to dissipating gravity waves in the mesopause region over the Andes, J. Geophys. Res.: Atmos., 126, https://doi.org/10.1029/2020jd033825, 2021.

Hines, C. O.: Internal atmospheric gravity waves at ionospheric heights, Can. J. Phys., 38, 1441–1481, https://doi.org/10.1139/p60-150, 1960.

Holton, J. R.: The influence of gravity wave breaking on the general circulation of the middle atmosphere, J. Atmos. Sci., 40, 2497–2507, https://doi.org/10.1175/1520-0469(1983)040<2497:Tiogwb>2.0.Co;2, 1983.

Jandreau, J. and Chu, X.: Baseline climatology of gravity waves From ~30 to ~70 km established with lidar observations over a decade at McMurdo (77.84°S, 166.67°E), Antarctica: implications for vertical wave evolution, Earth Space Sci., 13, https://doi.org/10.1029/2025ea004435, 2026.

Jandreau, J., Chu, X., Chen, Y., and Gardner, C. S.: Gravity wave energy baselines (~30–110 km) established from lidar observations at McMurdo (77.84°S, 166.67°E), Antarctica: energy dissipation and constituent diffusion, Geophys. Res. Lett., 53, https://doi.org/10.1029/2026gl124048, 2026.

Li, Q., Xu, J., Liu, H., Liu, X., and Yuan, W.: How do gravity waves triggered by a typhoon propagate from the troposphere to the upper atmosphere?, Atmos. Chem. Phys., 22, 12077–12091, https://doi.org/10.5194/acp-22-12077-2022, 2022a.
Li, T., She, C. Y., Liu, H. L., and Montgomery, M. T.: Evidence of a gravity wave breaking event and the estimation of the wave characteristics from sodium lidar observation over Fort Collins, CO (41°N, 105°W), Geophys. Res. Lett., 34, https://doi.org/10.1029/2006gl028988, 2007.
Li, T., Ban, C., Fang, X., Li, F., Cen, Y., Lai, D., Sun, C., Sun, L., Zhang, J., and Xu, C.: Seasonal variation in gravity wave momentum and heat fluxes in the mesopause region observed by sodium lidar, J. Geophys. Res.: Atmos., 127, https://doi.org/10.1029/2022jd037558, 2022b.
Lindzen, R. S.: Turbulence and stress owing to gravity wave and tidal breakdown, J. Geophys. Res.: Oceans, 86, https://doi.org/10.1029/JC086iC10p09707, 1981.
Liu, A. Z.: Estimate eddy diffusion coefficients from gravity wave vertical momentum and heat fluxes, Geophys. Res. Lett., 36, https://doi.org/10.1029/2009gl037495, 2009.
Liu, H. L.: Temperature changes due to gravity wave saturation, J. Geophys. Res.: Atmos., 105, 12329–12336, https://doi.org/10.1029/2000JD900054, 2000.
Liu, H. L.: Effective vertical diffusion by atmospheric gravity waves, Geophys. Res. Lett., 48, https://doi.org/10.1029/2020gl091474, 2021.
Liu, H. L., Hays, P. B., and Roble, R. G.: A numerical study of gravity wave breaking and impacts on turbulence and mean state, J. Atmos. Sci., 56, 2152–2177, https://doi.org/10.1175/1520-0469(1999)056<2152:ANSOGW>2.0.CO;2, 1999.
Liu, H. L., Lauritzen, P. H., Vitt, F., and Goldhaber, S.: Assessment of gravity waves from tropopause to thermosphere and ionosphere in high-resolution WACCM-X simulations, Journal of Advances in Modeling Earth Systems, 16, https://doi.org/10.1029/2023ms004024, 2024.
Liu, H. L., McInerney, J. M., Santos, S., Lauritzen, P. H., Taylor, M. A., and Pedatella, N. M.: Gravity waves simulated by high-resolution Whole Atmosphere Community Climate Model, Geophys. Res. Lett., 41, 9106–9112, https://doi.org/10.1002/2014gl062468, 2014a.
Liu, H. L., Bardeen, C. G., Foster, B. T., Lauritzen, P., Liu, J., Lu, G., Marsh, D. R., Maute, A., McInerney, J. M., Pedatella, N. M., Qian, L., Richmond, A. D., Roble, R. G., Solomon, S. C., Vitt, F. M., and Wang, W.: Development and validation of the Whole Atmosphere Community Climate Model with thermosphere and ionosphere extension (WACCM-X 2.0), Journal of Advances in Modeling Earth Systems, 10, 381–402, https://doi.org/10.1002/2017ms001232, 2018.
Liu, X., Xu, J., Yue, J., and Kogure, M.: Persistent layers of enhanced gravity wave dissipation in the upper mesosphere revealed from SABER observations, Geophys. Res. Lett., 49, https://doi.org/10.1029/2021gl097038, 2022.
Liu, X., Xu, J., Yue, J., and Liu, H.: Gravity-wave-perturbed wind shears derived from SABER temperature observations, Atmos. Chem. Phys., 20, 14437–14456, https://doi.org/10.5194/acp-20-14437-2020, 2020.
Liu, X., Xu, J., Yue, J., and Vadas, S. L.: Numerical modeling study of the momentum deposition of small amplitude gravity waves in the thermosphere, Ann. Geophys., 31, 1–14, https://doi.org/10.5194/angeo-31-1-2013, 2013.
Liu, X., Xu, J., Yue, J., Yuan, T., She, C. Y., and Vital, L. F. R.: Assessments the long-term stability of the SABER temperature measurement in the middle latitude MLT region, J. Geophys. Res.: Space Phys., 131, https://doi.org/10.1029/2025ja034476, 2026.
Liu, X., Yue, J., Xu, J., Wang, L., Yuan, W., Russell III, J. M., and Hervig, M. E.: Gravity wave variations in the polar stratosphere and mesosphere from SOFIE/AIM temperature observations, J. Geophys. Res.: Atmos., 119, 7368–7381, https://doi.org/10.1002/2013jd021439, 2014b.
Liu, X., Yue, J., Xu, J., Garcia, R. R., Russell III, J. M., Mlynczak, M., Wu, D. L., and Nakamura, T.: Variations of global gravity waves derived from 14 years of SABER temperature observations, J. Geophys. Res.: Atmos., 122, 6231–6249, https://doi.org/10.1002/2017jd026604, 2017.
Lu, X., Chu, X., Li, H., Chen, C., Smith, J. A., and Vadas, S. L.: Statistical characterization of high-to-medium frequency mesoscale gravity waves by lidar-measured vertical winds and temperatures in the MLT, J. Atmos. Sol. Terr. Phys., 162, 3–15, https://doi.org/10.1016/j.jastp.2016.10.009, 2017.

Malavart, A., Hoffmann, A., Bräuer, F., Hofmann, J., Hélière, A., Carnicero Dominguez, B., Friedl-Vallon, F., Sinnhuber, B.-M., Preusse, P., Walker, K., Riel, S., Keim, C., Schweikle, S., Nikolov, S., Belloc, C., St-Amand, C., Loew, H., Krisch, I., Sandri, P., Moser, K., Klimaszewski, M., Posselt, W., Giaccari, P., Caullier, F., and Abdon, S.: EE-11 candidate mission CAIRT: an overview of the Phase 0 and system studies, Proc. SPIE, 13667, 136990C, https://doi.org/10.1117/12.3077175, 2025.

Mlynczak, M. G. and Solomon, S.: A detailed evaluation of the heating efficiency in the middle atmosphere, J. Geophys. Res.: Atmos., 98, 10517–10541, https://doi.org/10.1029/93JD00315, 1993.

Mlynczak, M. G., Hunt, L. A., Russell III, J. M., and Marshall, B. T.: Updated SABER night atomic oxygen and implications for SABER ozone and atomic hydrogen, Geophys. Res. Lett., 45, 5735–5741, https://doi.org/10.1029/2018gl077377, 2018.

Mlynczak, M. G., Hunt, L. A., Garcia, R., Lopez-Puertas, M., Mertens, C. J., Nowak, N., and Marshall, B. T.: Energy Conservation in the Cooling and Contracting Upper Mesosphere and Lower Thermosphere, Geophys. Res. Lett., 51, https://doi.org/10.1029/2024gl109757, 2024.

Mlynczak, M. G., Hunt, L. A., Garcia, R. R., Harvey, V. L., Marshall, B. T., Yue, J., Mertens, C. J., and Russell III, J. M.: Cooling and contraction of the mesosphere and lower thermosphere from 2002 to 2021, J. Geophys. Res.: Atmos., 127, https://doi.org/10.1029/2022jd036767, 2022.

Mlynczak, M. G., Marshall, B. T., Garcia, R. R., Hunt, L., Yue, J., Harvey, V. L., Lopez-Puertas, M., Mertens, C., and Russell III, J. M.: Algorithm stability and the long-term geospace data record from TIMED/SABER, Geophys. Res. Lett., 50, https://doi.org/10.1029/2022gl102398, 2023.

Mlynczak, M. G., Daniels, T., Hunt, L. A., Yue, J., Marshall, B. T., Russell III, J. M., Remsberg, E. E., Tansock, J., Esplin, R., Jensen, M., Shumway, A., Gordley, L., and Yee, J. H.: Radiometric stability of the SABER instrument, Earth Space Sci., 7, https://doi.org/10.1029/2019ea001011, 2020.

Ortland, D. A. and Alexander, M. J.: Gravity wave influence on the global structure of the diurnal tide in the mesosphere and lower thermosphere, J. Geophys. Res.: Space Phys., 111, https://doi.org/10.1029/2005ja011467, 2006.

Remsberg, E. E., Marshall, B. T., Garcia-Comas, M., Krueger, D., Lingenfelser, G. S., Martin-Torres, J., Mlynczak, M. G., Russell III, J. M., Smith, A. K., Zhao, Y., Brown, C., Gordley, L. L., Lopez-Gonzalez, M. J., Lopez-Puertas, M., She, C. Y., Taylor, M. J., and Thompson, R. E.: Assessment of the quality of the Version 1.07 temperature-versus-pressure profiles of the middle atmosphere from TIMED/SABER, J. Geophys. Res.: Atmos., 113, https://doi.org/10.1029/2008jd010013, 2008.

Russell III, J. M., Mlynczak, M. G., Gordley, L. L., Tansock, J., J. J., and Esplin, R. W.: Overview of the SABER experiment and preliminary calibration results, Proceedings Volume 3756, Optical Spectroscopic Techniques and Instrumentation for Atmospheric and Space Research III, https://doi.org/10.1117/12.366382, 1999.

Siskind, D. E., Eckermann, S. D., McCormack, J. P., Alexander, M. J., and Bacmeister, J. T.: Hemispheric differences in the temperature of the summertime stratosphere and mesosphere, J. Geophys. Res.: Atmos., 108, https://doi.org/10.1029/2002jd002095, 2003.

Smith, A. K.: Physics and chemistry of the mesopause region, J. Atmos. Sol. Terr. Phys., 66, 839–857, https://doi.org/10.1016/j.jastp.2004.01.032, 2004.

Strelnikova, I., Baumgarten, G., and Lübken, F.-J.: Advanced hodograph-based analysis technique to derive gravity-wave parameters from lidar observations, Atmos. Meas. Tech., 13, 479–499, https://doi.org/10.5194/amt-13-479-2020, 2020.

Su, L., Collins, R. L., Krueger, D. A., and She, C.-Y.: Statistical Analysis of Sodium Doppler Wind–Temperature Lidar Measurements of Vertical Heat Flux, J. Atmos. Oceanic Technol., 25, 401–415, https://doi.org/10.1175/2007jtecha915.1, 2008.

Tao, X. and Gardner, C. S.: Heat flux observations in the mesopause region above Haleakala, Geophys. Res. Lett., 22, 2829–2832, 1995.

Torrence, C. and Compo, G. P.: A Practical Guide to Wavelet Analysis, Bull. Am. Meteorol. Soc., 79, 61–78, https://doi.org/10.1175/1520-0477(1998)079<0061:Apgtwa>2.0.Co;2, 1998.

Vadas, S. L.: Compressible f-plane solutions to body forces, heatings, and coolings, and application to the primary and secondary gravity waves generated by a deep convective plume, J. Geophys. Res.: Space Phys., 118, 2377–2397, https://doi.org/10.1002/jgra.50163, 2013.

Vadas, S. L. and Fritts, D. C.: Thermospheric responses to gravity waves: Influences of increasing viscosity and thermal diffusivity, J. Geophys. Res.: Atmos., 110, https://doi.org/10.1029/2004jd005574, 2005.
Vadas, S. L., Fritts, D. C., and Alexander, M. J.: Mechanism for the Generation of Secondary Waves in Wave Breaking Regions, J. Atmos. Sci., 60, 194–214, 2003.
Vadas, S. L., Zhao, J., Chu, X., and Becker, E.: The excitation of secondary gravity waves from local body forces: theory and observation, J. Geophys. Res.: Atmos., 123, 9296–9325, https://doi.org/10.1029/2017jd027970, 2018.
Walterscheid, R. L.: Dynamical cooling induced by dissipating internal gravity waves, Geophys. Res. Lett., 8, 1235–1238, https://doi.org/10.1029/GL008i012p01235, 1981.
Wang, L. and Alexander, M. J.: Global estimates of gravity wave parameters from GPS radio occultation temperature data, J. Geophys. Res.: Atmos., 115, https://doi.org/10.1029/2010jd013860, 2010.
Weinstock, J.: Heat flux induced by gravity waves, Geophys. Res. Lett., 10, 165–167, https://doi.org/10.1029/GL010i002p00165, 1983.
Wu, X., Zhu, Y., Smith, A. K., Kaufmann, M., Jiang, G., Liu, S., and Xu, J.: A new data set of nighttime chemical heating rates in the upper mesosphere and lower thermosphere derived from SCIAMACHY OH (9–6) emissions and SABER profiles, Atmos. Chem. Phys., 26, 4669–4683, https://doi.org/10.5194/acp-26-4669-2026, 2026.
Xu, J., Smith, A. K., and Ma, R.: A numerical study of the effect of gravity-wave propagation on minor species distributions in the mesopause region, J. Geophys. Res.: Atmos., 108, https://doi.org/10.1029/2001jd001570, 2003.
Xu, J., Liu, H. L., Yuan, W., Smith, A. K., Roble, R. G., Mertens, C. J., Russell III, J. M., and Mlynczak, M. G.: Mesopause structure from Thermosphere, Ionosphere, Mesosphere, Energetics, and Dynamics (TIMED)/Sounding of the Atmosphere Using Broadband Emission Radiometry (SABER) observations, J. Geophys. Res.: Atmos., 112, https://doi.org/10.1029/2006jd007711, 2007.
Xu, J., Smith, A. K., Liu, H. L., Yuan, W., Wu, Q., Jiang, G., Mlynczak, M. G., and Russell III, J. M.: Estimation of the equivalent Rayleigh friction in mesosphere/lower thermosphere region from the migrating diurnal tides observed by TIMED, J. Geophys. Res.: Atmos., 114, https://doi.org/10.1029/2009jd012209, 2009.
Xue, X. H., Liu, H. L., and Dou, X. K.: Parameterization of the inertial gravity waves and generation of the quasi-biennial oscillation, J. Geophys. Res.: Atmos., 117, https://doi.org/10.1029/2011jd016778, 2012.
Yamashita, C., England, S. L., Immel, T. J., and Chang, L. C.: Gravity wave variations during elevated stratopause events using SABER observations, J. Geophys. Res.: Atmos., 118, 5287–5303, https://doi.org/10.1002/jgrd.50474, 2013.
Yiğit, E. and Medvedev, A. S.: Heating and cooling of the thermosphere by internal gravity waves, Geophys. Res. Lett., 36, https://doi.org/10.1029/2009gl038507, 2009.
Yue, J. and Wang, N.: Estimation of adiabatic cooling and warming in the mesosphere and lower thermosphere, J. Atmos. Sol. Terr. Phys., 269, https://doi.org/10.1016/j.jastp.2025.106492, 2025.